In Situ Engineering of Inorganic-Rich Solid Electrolyte Interphases via Anion Choice Enables Stable, Lithium Anodes

Jason A. Weeks, James N. Burrow, Jiefeng Diao, Austin G. Paul-Orecchio, Hrishikesh S. Srinivasan, Rinish Reddy Vaidyula, Andrei Dolocan, Graeme Henkelman, and C. Buddie Mullins*

The discovery of liquid battery electrolytes that facilitate the formation of stable solid electrolyte interphases (SEIs) to mitigate dendrite formation is imperative to enable lithium anodes in next-generation energy-dense batteries. Compared to traditional electrolyte solvents, tetrahydrofuran (THF)-based electrolyte systems have demonstrated great success in enabling high-stability lithium anodes by encouraging the decomposition of anions (instead of organic solvent) and thus generating inorganic-rich SEIs. Herein, by employing a variety of different lithium salts (i.e., $LiPF_6$, LiTFSI, LiFSI, and LiDFOB), it is demonstrated that electrolyte anions modulate the inorganic composition and resulting properties of the SEI. Through novel analytical time-of-flight secondary-ion mass spectrometry methods, such as hierarchical clustering of depth profiles and compositional analysis using integrated yields, the chemical composition and morphology of the SEIs generated from each electrolyte system are examined. Notably, the LiDFOB electrolyte provides an exceptionally stable system to enable lithium anodes, delivering >1500 cycles at a current density of 0.5 mAh g^{-1} and a capacity of 0.5 mAh g^{-1} in symmetrical cells. Furthermore, Li//LFP cells using this electrolyte demonstrate high-rate, reversible lithium storage, supplying 139 mAh $g_{(LFP)}^{-1}$ at C/2 ($\approx$0.991 mAh cm^{-2}, @ 0.61 mA cm^{-2}) with 87.5% capacity retention over 300 cycles (average Coulombic efficiency >99.86%).

1. Introduction

Unprecedented societal demand for lightweight, rechargeable energy storage technologies has been prompted by expansion in the harvesting of renewable energy, increased energy requirements for consumer products, and electrification of the transportation sector. To meet these demands, lithium battery chemistries and cell designs with greater energy density are required, yet lithium storage chemistries have remained nearly identical for the majority of the technology's lifetime, employing a graphite anode and a transition metal oxide or polyanion cathode.[1] On the other hand, thin lithium-metal anodes with a planar, non-dendritic electroplating morphology hold promise to enable high energy density Li^+ storage, providing a high theoretical capacity (3860 mAh g^{-1}, 2016 mAh cm^{-3}) and the lowest achievable reduction potential (-3.04 V vs SHE) available.[2]

A central hurdle for implementing lithium-metal anodes is the often dendritic electrodeposition morphology, which upon substantial growth, can pierce through the separator and result in electrical short-circuiting or catastrophic failures. A leading theory implicates limitations in Li^+ diffusion as the root of dendritic lithium growth.[3–6] After a specified time of Li plating at a given current density, polarization and Li^+ concentration depletion at the electrode surface are hypothesized to result in dendrite formation. This characteristic "Sand's time" (τ_s) quantifies the current-dependent time when the lithium-ion concentration near the electrode surface decreases to zero aEfter which uniform

J. A. Weeks, J. Diao, A. G. Paul-Orecchio, R. R. Vaidyula, G. Henkelman, C. B. Mullins
Department of Chemistry
The University of Texas at Austin
Austin, TX 78712-1224, USA
E-mail: mullins@che.utexas.edu

J. N. Burrow, H. S. Srinivasan, C. B. Mullins
John J. McKetta Department of Chemical Engineering
The University of Texas at Austin
Austin, TX 78712-1589, USA

J. Diao, G. Henkelman
Oden Institute for Computational Engineering and Sciences
The University of Texas at Austin
Austin, TX 78712, USA

A. Dolocan, C. B. Mullins
Texas Materials Institute
The University of Texas at Austin
Austin, TX 78712-1591, USA

electroplating is prevented for a given electrolyte system.[6,7] Sand's time is described by Equation (1), where D is the ambipolar diffusion coefficient, e is the electronic charge, J is the current density, C_0 is the initial concentration, and μ_a and μ_c are the mobilities of the anions and cations, respectively. Furthermore, dendrite growth is often self

$$\tau_s = D\left(\frac{C_0 e z_c}{2J}\right)^2 \left(\frac{\mu_a + \mu_c}{\mu_a}\right)^2 \tag{1}$$

propagating since these perturbations cause the focusing of current density near the tip of the dendrite and induce nonuniform ionic flux at the surface of the electrode.[8–10] Mistry et al. demonstrated that the local Li$^+$ concentration could reach zero even before Sand's time due to the effects of heterogeneous solid electrolyte interphases (SEIs) on the surface energy and the resulting electrolyte confinement in high-surface area Li$^+$-deposition morphologies.[11] Therefore, electrolytes and SEIs with high cation mobility can withstand larger effective current densities without dendrite formation and promote stable cycling of lithium-metal anodes.

Another major hurdle for enabling the practical implementation of lithium-metal anodes is the formation of an SEI that is conducive to long-term, high current density cycling. The SEI is a passivation layer formed on the surface of the lithium-metal anode that plays a critical role in successful battery operation, acting as the liaison for lithium transport between the anode and the bulk electrolyte. An ideal SEI is a thin, ionically conductive yet electronically insulating layer comprised of a mosaic of the electrolyte reduction products at the anode.[12,13] Three major properties of the interphase influence the effectiveness of this passivation layer in mediating electrochemical cycling: (1) mechanical stability, (2) ion mobility, and (3) electronic resistivity (**Scheme 1**). The SEI requires both mechanical strength and ductility, requiring mechanical strength to withstand the normal force induced from lithium deposition and elasticity to withstand repeated expansion and contraction induced by the continual plating and stripping process.[14–18] Inability to withstand these processes results in the fracture of the SEI, thereby exposing unpassivated lithium. This newly exposed surface promotes nonuniform ionic flux, enabling dendrite formation and consuming the overall lithium inventory of the system by requiring additional electrolyte decomposition for passivation.[3,5] As the mediator for ion transport from the electrolyte to the bulk lithium, the SEI and its effects on Li$^+$ mobility can significantly impact the electrochemical performance of the system. Furthermore, the lithiophilicity of the SEI constituents can directly impact the kinetics of lithium plating by influencing desolvation energy and Li$^+$ transport.[19–21] Electronic resistivity is an inherent property of an SEI as it acts as the insulating layer to prevent electron tunneling between the electrolyte and the anode. Increasing the electronic resistivity of the SEI can minimize the required electron tunneling distance,[22,23] thereby enabling thin SEIs, which reduce the consumption of lithium inventory and decrease the required distance for ion transport.[24] Numerous properties of the SEI, such as thickness, ionic conductivity, chemical/spatial uniformity, interfacial adhesion, and mechanical stability, have serious implications on the proclivity for dendrite growth by modulating the Li$^+$-ion flux and electrodeposition morphology. As a re-
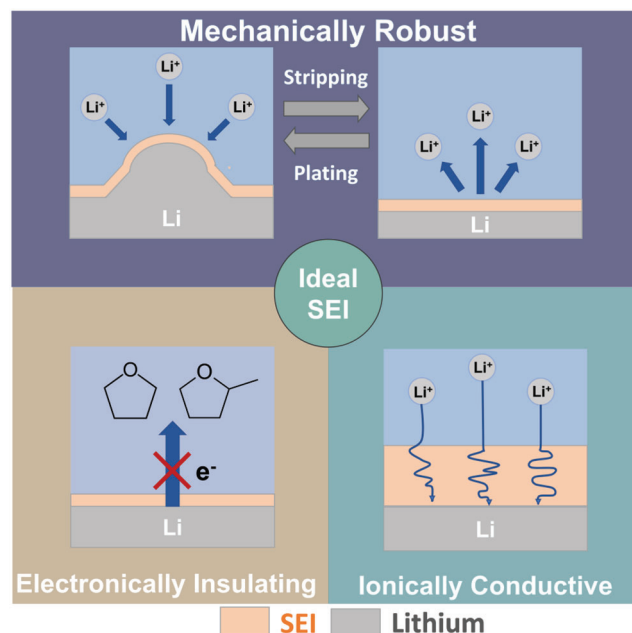
Scheme 1. Graphic depicting the ideal properties of a stable lithium-metal SEI.

sult, SEIs play a dominant role in determining the overpotential of plating/stripping, the degree of electrolyte degradation during cycling, and the effective lifetimes of the cell.[2,8,18,25–27]

For decades, suppression or complete elimination of lithium-metal dendrites has been pursued via purposeful engineering of the SEI. Recent computational studies, such as those by Spotte-Smith et al.,[28,29] have provided some insight into the mechanisms of the Li-mediated electrolyte decomposition reaction networks that lead to SEI formation. However, as electrolyte decomposition is a transient, kinetically controlled process occurring in an electrolyte with variable chemical composition due to solvent breakdown and Li$^+$ inventory consumption throughout cycling, a priori design of SEIs via electrolyte engineering presents a significant scientific challenge to enable implementation of LMBs. However, recent works investigating "locally high concentration electrolytes" (LHCE) have demonstrated significant success in establishing SEIs with properties favorable for long term-performance and low overpotentials.[30–33] The success of these systems is attributed to their tendency to form inorganically rich SEIs in situ. Inorganic species such as lithium fluorides, lithium carbonates, boron oxides, lithium borates, and lithium sulfides have chemical (ionic conductivity and electronic resistivity) and/or physical properties (rigidity and ductility) that are advantageous for the electrode's performance.[30,33,34] LHCEs produce inorganic-rich SEIs due to the high ionic aggregate (AGG) concentration and contact-ion pair (CIP) solvation moieties.[35–37] These motifs modulate the LUMO of both the solvent and anion molecules, making the lowest available energy level (most redox-active) that of the anion instead of the solvent.[38,39] Similar success has been demonstrated using high concentration (>3.5 M) electrolytes, as the high concentration of Li$^+$ forces the increased formation of AGGs and CIPs due lower global concentration of solvent available. The issue with these strategies is that

ADVANCED
SCIENCE NEWS
www.advancedsciencenews.com

ADVANCED
MATERIALS
www.advmat.de

the introduction of diluents or excessive salt content can negatively influence electrolyte transport properties, such as ionic conductivity and viscosity, and/or significantly increase the cost of the electrolyte.[36,38,39] On the other hand, weakly solvating electrolytes (WSEs), such as those composed of tetrahydrofuran (THF) and/or methyl tetrahydrofuran (m-THF), provide a considerable concentration of CIPs and AGGs even at traditional ($\approx$1 M) salt concentrations.[26,31,33] This unique solvation behavior is enabled by the low dielectric constant, low dipole moment, and single coordination site of THF ($\kappa = 7.58$, $D = 1.75$) and m-THF ($\kappa = 6.97$, $D = 1.38$).[40] These solvents provide a medium for creating electrolytes with favorable solvation properties with traditional concentrations, low viscosities, high ionic conductivities, and low cost. The impact of these AGG and CIP solvation motifs on the SEI composition and overall lithium-metal anode stability was examined previously by Lee et al. Still, the role of anion identity on the resulting properties of the salt-derived SEI has yet to be explored or understood.[33]

Employing a THF-mix solvent system demonstrated in previous literature to encourage anion-derived SEIs, we investigate how the identity of electrolyte anion impacts the chemical composition and morphology of the SEI and the resulting performance of lithium anodes. By studying four different electrolyte salts (LiPF$_6$, LiTFSI, LiFSI, and LiDFOB), we fine-tuned the chemical compositions and properties of SEIs on lithium anodes and thus generated a platform to study the effect of chemical speciation on cycling performance and lithium deposition morphology. Through electrochemical testing, we have demonstrated that the salt plays a prominent role in modulating the redox potential of the electrolyte and thus influences the decomposition pathways for SEI formation. Postmortem X-ray photoelectron spectroscopy (XPS) and depth profiling with time-of-flight secondary-ion mass spectrometry (ToF-SIMS) enabled a comprehensive investigation into the evolution of the SEI throughout the cycling of the cells. Furthermore, our study employs new methods of ToF-SIMS analysis, such as hierarchical clustering of depth profiles and compositional analysis using integrated yields, not previously employed in literature on lithium-metal anodes. Hierarchical clustering of the depth profiles for all identified species enables compositional relationships to be formed based on the similarities in the depth profile, unlocking a comprehensive view of the spatiochemical composition of each SEI. Compositional analysis using integrated yields enables a quantitative method for comparing SEI composition between samples and provides a measurable degree to determine chemical heterogeneity within the system. This study not only presents an analytical methodology to better allow the community to understand the composition of lithium-metal SEIs but also demonstrates the importance of anion selection for influencing the overall properties of the SEI. The results of this study demonstrate how a simple exchange of ionic salt can be the difference between a thick, unstable SEI and a thin, dense SEI capable of cycling for thousands of hours.

2. Results

2.1. Electrolyte Characterization

Various techniques were used to probe the viscosity, ionic conductivity, electrochemical stability window, and electrolyte solva-

Table 1. Viscosities and ionic conductivities of the various THF-mix electrolytes.

Electrolyte	Viscosity [mPa s]	Ionic conductivity [mS cm^{-1}]
LiPF$_6$	1.17	12.8
LiTFSI	1.31	6.72
LiFSI	1.29	5.82
LiDFOB	1.10	16.1

tion structures to establish a baseline for each system's inherent physical and chemical properties. Viscometric measurements reveal that the THF-mix solvent system offers a low-viscosity medium for lithium electrolyte solutions. The THF-mix electrolytes have lower viscosities than traditional electrolytes systems (e.g., 1 M LiPF$_6$ in EC: DMC, 1.92 cP) and high concentration electrolytes (>50 cP), with all electrolytes having a viscosity ranging from 1.10 to 1.31 cP (**Table 1**).[41] Viscosities of the electrolytes ranked from lowest to highest are as follows: LiDFOB < LiPF$_6$ < LiFSI < LiTFSI.

The ionic conductivity of both the SEI and the electrolyte plays a pivotal role in the formation and propagation of lithium dendrites during cycling; therefore, the ionic conductivities of these electrolytes were determined using electrochemical impedance measurements on a Pt/Pt cell configuration. The results of these measurements (Figure S1, Supporting Information) reveal that the anion selection affects the ionic conductivity of the electrolyte solution considerably. Ionic conductivities of the electrolytes ranked from highest to lowest are as follows: LiDFOB > LiPF$_6$ > LiTFSI > LiFSI (Table 1). Numerous chemical factors, such as solvation structures, ionic association, and the steric effects of ions, can influence ionic conductivity throughout a solution.[42] However, the similarity in the trend of the higher viscosity solvents yielding lower ionic conductivities in the THF-mix sample set suggests that the physical attributes of the solution play a significant role in the electrolyte's final conductivity.

Linear sweep voltammetry (LSV) determined the electrolyte solutions' oxidative and reductive electrochemical stability window. Oxidative LSV (Figure S2, Supporting Information) revealed the upper voltage electrochemical stability window, with most of the electrolytes demonstrating oxidative decomposition when exposed to applied potentials of $\geq$4.1 V (vs Li/Li$^+$). However, the LiDFOB electrolyte exhibited a slightly expanded stability window, where it oxidatively decomposes at $\approx$4.2 V. This voltage window limits the electrolytes' capability with high voltage cathode materials like NCM and NCA, but they provide a stable environment for polyanion cathodes such as LFP. Reductive voltammograms (**Figure 1**a) of the electrolyte systems expose the lower voltage stability and a glimpse at the electrochemical potentials where electrolyte decomposition reactions occur to form SEI. Reductive LSVs (Figure 1a) suggest that the THF-mix electrolytes have comparable reductive stability. Yet, taking the derivative of the reductive LSV curve (Figure 1b) shows their distinct difference in the electrochemical decomposition of the electrolytes. Ranked from least to most stable: LiFSI < LiTFSI < LiPF$_6$ < LiDFOB. Studies of LHCEs suggest that increased reductive stability windows can be linked to increased CIP and AGG solvation
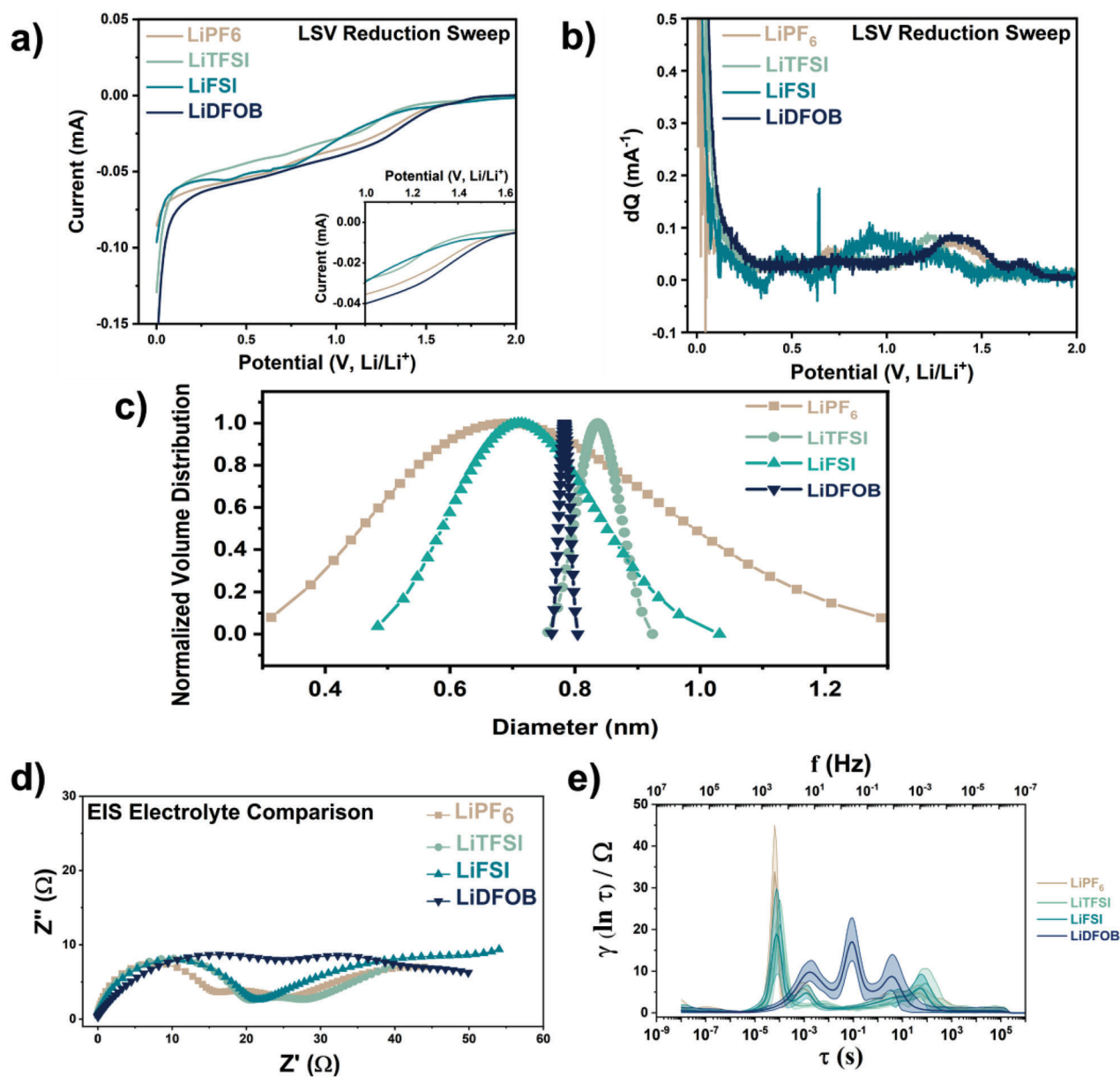
Figure 1. a) Size distribution of the THF-mix electrolytes obtained from fitting a spherical model on the solvent-subtracted SAXS data. electrolytes. b) Reductive linear voltage sweeps and c) their derivatives, showing the reductive stability of the THF-mix electrolytes. d) Nyquist plots of the various electrolytes obtained from EIS of the THF-mix systems after 10 cycles. e) DRT spectra transformation of the EIS spectra.

moieties, which may have implications on the preference for salt versus solvent decomposition and final SEI composition.[36,38]

Small-angle X-ray scattering (SAXS) was employed to further explore the Li+ solvation in these electrolytes. By obtaining the spectra of the various electrolytes and subtracting these results from the spectra of the THF-mix solvent (Figures S3 and S4, Supporting Information), the clusters pertaining to the solvation of the salt molecules were revealed (Figure S5, Supporting Information). Employing a spherical fitting model, the mean diameter of the major solvation nanostructures was determined (Figure 1c). These results show that the LiDFOB and LiTFSI salt create solvation nanostructures with a narrow volume size distribution, while the LiPF6 and LiFSI display a wide array of potential clustering sizes. Furthermore, the average size of the solvated clusters in the THF-mix electrolytes ranked from smallest to largest are as follows: LiPF6 < LiFSI < LiDFOB < LiTFSI. Previous studies have shown that larger solvation clusters are typically indicative of higher concentrations of AGG and CIP solvation motifs.[43,44]

2.2. Electrochemical Testing

Electrochemical impedance spectroscopy was conducted on all four electrolyte systems after the first, fifth, and tenth cycles of

**ADVANCED
SCIENCE NEWS**

www.advancedsciencenews.com

**ADVANCED
MATERIALS**

www.advmat.de

symmetrical cell plating/stripping to investigate the impedance of the electrolyte and the resulting SEI. The overall impedance of these cells decreased with continued electrochemical cycling (Figure S6, Supporting Information), likely due to an increase in the total electrochemically active surface area as lithium is plated and dendritic growths are formed throughout cycling. The electrolytes demonstrate different impedance spectra and peak shapes, yet the maximum real and imaginary impedance is comparable between all samples (Figure 1d). Distribution of relaxation times (DRT) was obtained from EIS spectra to further elucidate the difference between the impedance spectra of the electrolyte (Figures S8 and S9, Supporting Information). DRT is a valuable technique that can reveal the degree of resistance and frequency at which various electrochemical processes, such as SEI polarization, charge transfer, Li$^+$ desolvation, electrolyte reduction, and Li$^+$ transport, occur.[45] All of the electrolytes demonstrate three distinct peaks (i.e., low, mid, and high frequencies) in their spectra, a low, mid, and a high frequency in their spectra. Previous research attributes low-frequency resistances to transport and diffusive processes, medium-frequency resistances to Li$^+$ desolvation and charge transfer, and high-frequency processes to the ohmic polarization of the SEI.[46] As expected, the electrolytes show minimal changes in their DRT spectra per cycle basis (Figure S8, Supporting Information). Comparing between electrolytes (Figure 1e), the LiPF6, LiTFSI, and LiFSI systems all show very similar DRT spectra with three distinct processes at $\approx10^{3.5}$, $\approx10^{2.5}$, and $\approx10^{-2.5}$ s, respectively, whereas the LiDFOB demonstrates very different timescales for its' three features, $\approx10^2$, $\approx10^{0.5}$, and $\approx10^{-1.5}$. Additionally, these three electrolytes demonstrate significant resistance at their highest and lowest frequency processes. At the same time, the LiDFOB system displays significantly lower resistance for these processes but a large resistance for its mid-frequency process. Interestingly, a change in the salt composition of an electrolyte and the resulting SEI composition could impact the timescales and resistances of these fundamental processes to such a significant degree. We believe this result should be investigated in future studies as it may uncover a unique fundamental insight for adjusting the inherent electrochemical properties of lithium-metal anode electroplating.

The stability and reversibility of Li electrodeposition in these electrolyte systems were quantified using symmetrical cells through long-term performance testing. Low- (0.5 mA cm^{-2}, 0.5 mAh cm^{-2}) (**Figure 2**a) and high current stability testing (1.0 mA cm^{-2}, 1.0 mAh cm^{-2}) (Figure 2b) were conducted until cell failure. For all electrolytes and current densities, examination of the voltage profiles (Figures S10 and S11, Supporting Information) implied a lack of short circuiting until cell failure, depicting distinct features (e.g., nucleation, mass transfer limitation) during the stripping and plating process.[3,8] The LiPF6 system demonstrated the worst stability, producing variable overpotentials during low current density testing and unstable cycling and failure during high current testing. After 25 cycles at 0.5 mA cm^{-2}, the voltage curves observed for the cell with LiPF6 electrolyte transitioned from initially unstable overpotentials (≈100 mV) towards overpotentials circa 50 mV for ≈200 stable cycles (Figure 2a). The initial unstable cycles likely correspond to the SEI's continual formation and/or structural reorganization. Subsequently, the overpotential rose each cycle until eventual cell failure after
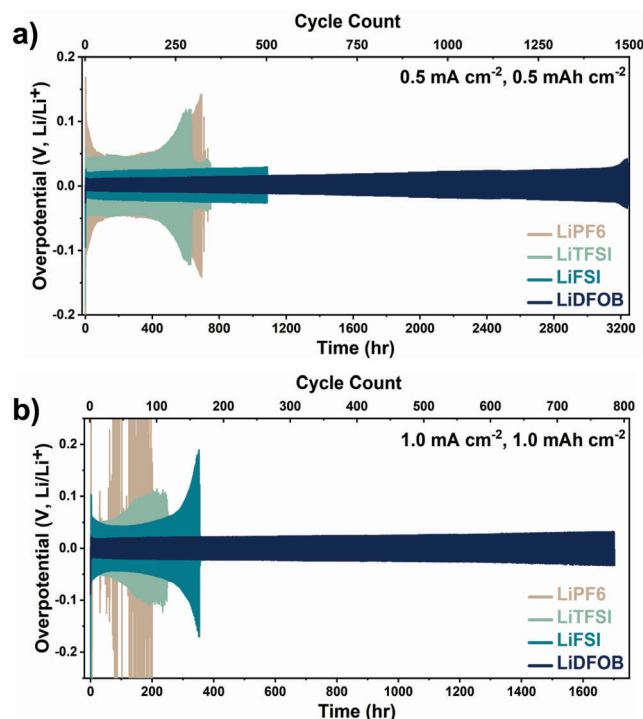
Figure 2. a,b) Long-term stability testing of symmetrical cells of the various THF-mix electrolyte systems under low current density conditions (0.5 mAh cm^{-2}, 0.5 mA cm^{-2}) (a) and high current density conditions (1.0 mAh cm^{-2}, 1.0 mA cm^{-2}) (b).

≈320 cycles (700 h). At the larger current densities (1.0 mA cm^{-2}), the LiPF$_6$ system exhibits unstable cycling almost immediately, showing large peaks in overpotential, which can be attributed to the formation of dead lithium and dendrite fracture within the cell (Figure 2b).[31] Compared to the LiPF$_6$ system, the LiTFSI electrolyte system at 0.5 mA cm^{-2} demonstrates improved stability, exhibiting moderate overpotentials (≈40 mV) (Figure 2a) until ≈225 cycles where overpotentials began to increase before cell failure at 625 h (≈275 cycles). High current density cycling, at 1.0 mA cm^{-2}, shows similar stability where LiTFSI cycled stably for 300 h (≈135 cycles) before increases in overpotential and failure at 350 h (≈160 cycles) (Figure 2b), likely indicating dendrite propagation and short. The LiFSI electrolyte enables more stable plating/stripping at 0.5 mA cm^{-2} than LiPF$_6$ or LiTFSI, achieving over ≈500 cycles with only ≈20 mV of overpotential (Figure 2a). High-rate testing (Figure 2b) showed the LiFSI electrolyte also depicted stable cycling for over 600 h (≈250 cycles) with a modest overpotential of ≈45 mV. Supporting the validity of this study, our LiFSI electrolyte reproduces performance metrics observed in other studies employing this system.[31,32] Of the four electrolytes studied, the LiDFOB system exhibited the best performance, demonstrating stable cycling for over 3200 h (≈1500 cycles) with minimal overpotentials (≈10 mV) at 0.5 mA cm^{-2} cycling (Figure 2a) and for over 1600 h (≈775 cycles) with an overpotential of ≈20 mV at 1.0 mA cm^{-2} (Figure 2b). At both current densities, the LiDFOB system displays low, consistent overpotentials throughout cycling with only a minor increase in overpotential.

**ADVANCED
SCIENCE NEWS**

www.advancedsciencenews.com

**ADVANCED
MATERIALS**

www.advmat.de
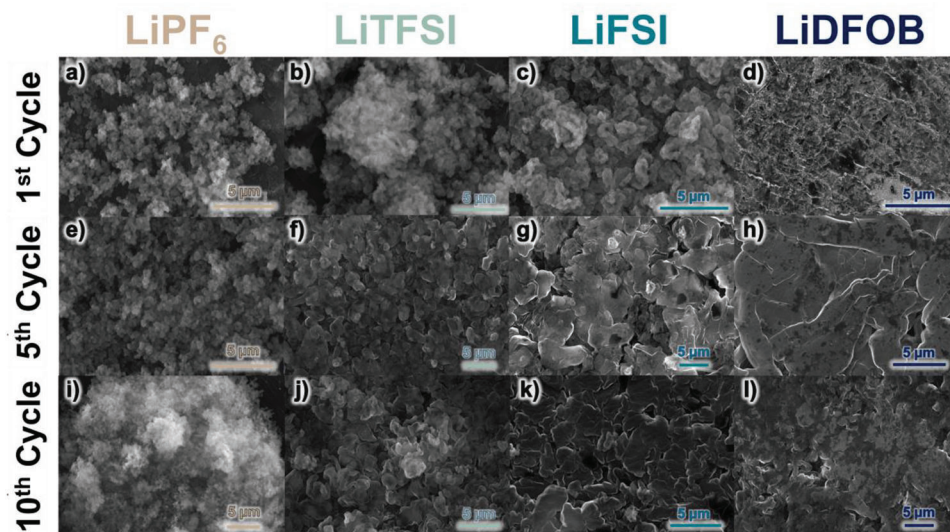
Figure 3. a–l) Postmortem microscopy images depicting the lithium electrodes from the LiPF$_6$ (a,e,i), LiTFSI (b,f,j), LiFSI (c,g,k), and LiDFOB (d,h,l) systems after the 1st (a–d), 5th (e–h), and 10th (i–l) cycles, respectively. The electrodes shown were cycled at 1 mA cm^{-2} to a capacity of 1 mAh cm^{-2}.

Overall, these electrolytes demonstrate distinctly different electrochemical stability. In general, the LiPF6 electrolyte depicts the lowest plating/stripping stability, unable to cycle effectively at large current densities. The LiTFSI and LiFSI electrolytes both provide moderate cycle life, but the LiFSI demonstrates smaller overpotentials and increased longevity compared to LiTFSI. Finally, the LiDFOB system provides not only exceptionally low overpotentials but also a cycle life that is nearly three times that of the LiFSI system.

2.3. Postmortem Scanning Electron Microscopy (SEM)

Lithium deposition morphology impacts lithium-metal anodes' overall efficiency and long-term stability. Generally, low surface area (SA): volume ratio morphologies perform better due to two significant factors: (1) high SA depositions create thinner, mechanically weaker dendritic structures.[18,47] (2) Additional SEI formation (electrolyte decomposition) is required to sufficiently passivate structures with larger SA, resulting in losses in overall efficiency and lithium inventory in the cell.[5,27,48] Postmortem microscopy images of electrodes from symmetrical cells, shown in **Figure 3**, depict the morphology of the freshly deposited lithium after the first, fifth, and tenth cycles, respectively. From the LiPF$_6$ electrolyte, lithium was initially deposited nonuniformly across the anode surface (Figure S12a, Supporting Information) as dendrites with a thin, "necklace-like" morphology (Figure 3a). Continued cycles of plating and stripping resulted in high surface area "cloud-like" dendrite formations that were distributed more uniformly across the electrode area (Figure 3b,c). These dendrite morphologies with ultra-high surface areas are conducive to the formation of dead lithium and lead to unstable stripping/plating, similar to the results seen in the high-current density cycling.[18,47] The LiTFSI system also exhibited heterogeneous deposition after initial Li$^+$ plating, but the dendrites appeared to have morphologies with decreased SA compared to those observed when employing LiPF$_6$ (Figure 3b). Continued plating and stripping with this LiTFSI electrolyte increased the spatial uniformity of lithium growth across the electrode surface, but the size/thickness of these formations was highly variable (Figure 3f,k). In contrast, lithium plating/stripping with the LiFSI electrolyte demonstrated lower "cluster-like" depositions (Figure 3c) uniformly across the surface of the electrode after the first cycle (Figure S12c, Supporting Information). Continued cycling further promoted the growth of these lithium depositions, eventually resulting in a homogeneous, densely-packed morphology across the electrode surface (Figure 3g,k). Finally, for the LiDFOB electrolyte, a near-optimal lithium deposition morphology was observed throughout cycling, uniformly covering the entire electrode surface (Figure S12d, Supporting Information) and generating sheet-like structures (Figure 3d) with extremely low SA. This morphology was retained throughout cycling, and enhanced lithium packing was observed as the plating and stripping process repeated (Figure 3h,l).

These results are further supported by macroscopic visualization of the electrodes after the first (Figure S12, Supporting Information) and tenth cycle (Figure S13, Supporting Information). The LiPF$_6$ and LiTFSI systems demonstrate heterogeneous deposition of lithium macroscopically, with some areas of the electrodes having little to no lithium plating after the initial cycle. Meanwhile, the LiFSI and LiDFOB systems demonstrate uniform lithium plating and maintain structures with low SA throughout cycling, as seen in Figure 3. In all, SEM analysis after continual cycling with the various electrolyte systems revealed that the surface area of the deposition morphologies followed the trend of LiPF$_6$ >> LiTFSI > LiFSI > LiDFOB.

2.4. X-ray Photoelectron Spectroscopy (XPS)

XPS was employed to analyze the chemical environment of the SEIs generated on the lithium anodes after completing each

**ADVANCED
SCIENCE NEWS**

www.advancedsciencenews.com

**ADVANCED
MATERIALS**

www.advmat.de

electrolyte system's first, fifth, and tenth cycles. XPS provides an effective method for quantifying the chemical species found within the postmortem electrodes; however, the limited probe depth of this technique limits its ability to provide chemical information about the entirety of the SEI. Therefore, XPS is employed to: (1) identify key species in the SEI and (2) quantify how the chemical composition of the SEIs changes throughout cycling. Survey scans of these electrodes (Figure S14, Supporting Information) verified the integrity of the testing procedures and electrolytes, depicting only the expected elemental compositions with no signs of contamination from unknown species.

High-resolution scans were conducted in the regions of binding energy relevant for each of the chemical species, such as the C 1s (**Figure 4**a,e,i,m; Figure S15, Supporting Information), O 1s (Figure 4b,f,j,n; Figure S16, Supporting Information), F 1s (Figure 4c,g,k,o,; Figure S17, Supporting Information), P 2p (Figure 4d; Figure S18, Supporting Information), S 2p (Figure 4h,l; Figure S19, Supporting Information), and B 1s (Figure 4p; Figure S20, Supporting Information), regions. Comparing the XPS spectra of the $LiPF_6$ (Figure 4a–d), LiTFSI (Figure 4e–h), LiFSI (Figure 4i–l), and LiDFOB (Figure 4m–p) derived SEIs highlights the significant difference in decomposition products resulting from these electrolytes. The specific parameters used for peak/species determination can be found in the experimental section of the supporting information. A complete analysis of the XPS results in the context of resulting lithium anode performance can be found later in this manuscript in the discussion section. Further details on the experimental parameters and data processing can be found in the Supporting Information.

Furthermore, the quantification of the atomic composition of each SEI is shown in Figure 4q. The SEI generated from the $LiPF_6$ electrolyte contained a large proportion of inorganic species after the first cycle (13.2 at% of heteroatoms (or non-Li species)), but the continual decrease in inorganic composition throughout cycling (fifth cycle = 5.7 at%, tenth cycle = 4.5 at%) suggested instability of the SEI. Interestingly, the opposite trend was seen in the LiTFSI system, where the SEI initially demonstrated a very low inorganic composition (5.8 at%, of heteroatoms) that steadily grew throughout cycling (fifth cycle = 7.3 at%, tenth cycle = 13.2 at%). On the other hand, the LiFSI and LiDFOB systems showed relatively stable elemental composition throughout cycling, with only slight growth in the C and O species as cycling progressed. After the first cycle, the LiFSI system demonstrated moderate inorganic composition with a heteroatom content of 8.1 at%. The LiDFOB electrolyte produced an SEI extremely rich in inorganics (19.7 at%, of heteroatoms), and only a slight, subtle decrease of inorganics was observed as cycling continued (fifth cycle = 19.1 at%, tenth cycle = 17.8 at%). A tabulated summary of the atomic quantification obtained from the XPS analysis throughout the cycling process can be found in Tables S1 and S2 in the Supporting Information.

2.5. Time-of-Flight Secondary-Ion Mass Spectrometry (ToF-SIMS)

ToF-SIMS was employed to provide a spatially resolved depth profile of the composition of the various SEIs generated from the different electrolyte systems. SEIs are notoriously chemically complex due to the variety of diverse decomposition reactions that

can occur between the electrolyte and the lithium anode. ToF-SIMS analysis of SEIs provides overwhelming information, generating depth profiles with hundreds of ions for each sample. A majority of studies employing this technique merely examine the depth profiles of certain molecules/ions deemed significant a priori (i.e., from other analytical techniques). However, a more thorough and unbiased examination of ToF-SIMs data could improve our understanding of these chemically-complex SEIs. To utilize as much information as possible when analyzing our systems, we employed a more holistic analysis, employing hierarchical clustering of the depth profiles of all species/peaks identified from the mass spectra of each SEI to enable binning of ions with similar depth profiles. The complete mass spectra for the $LiPF_6$, LiTFSI, LIFSI, and LiDFOB samples are displayed in Figures S21–S25 (Supporting Information), respectively. Using specific constraints for peak identification, detailed in the experimental methods section, with 141, 134, 114, and 72 individual species being identified in the mass spectra of the $LiPF_6$, LiTFSI, LiFSI, and LiDFOB SEIs, respectively (Figure S56, Supporting Information). It should be noted that the LiTFSI and LiFSI electrolytes share many of the same decomposition products, likely due to their analogous chemical structure. The clustering of the spectra was enabled with the Broad Institutes' open-source Morpheus software (https://software.broadinstitute.org/morpheus, Broad Institute. Depictions of the calculated hierarchical relationship between the ions of the $LiPF_6$ (Figure S25, Supporting Information), LiTFSI (Figure S26, Supporting Information), LIFSI (Figure S27, Supporting Information), and LiDFOB (Figure S28, Supporting Information) samples can be found in the supporting information. Furthermore, correlation plots of the detected ions in the $LiPF_6$ (Figure S29, Supporting Information), LiTFSI (Figure S30, Supporting Information), LIFSI (Figure S31, Supporting Information), and LiDFOB (Figure S32, Supporting Information) spectra can also be found in the supporting information. Hierarchical clustering was employed to demonstrate similarities in the various ions' depth profiles and aid in chemical identification. Depth profiles of the various ions (grouped in their respective clusters) found in the $LiPF_6$, LiTFSI, LIFSI, and LiDFOB are shown in Figures S33–S36 (Supporting Information), respectively. For full details discussing the criteria for peak selection and parameters used for the spectra clustering analysis, please see the Experimental Section in the Supporting Information.

The clustering analysis reveals some interesting trends by providing insight into the regions of the SEI, the thicknesses of these regions, and enabling the creation of a complete spatiochemical profile for each SEI. Denoted by the clustering analysis, there appear to be four distinct regions in each of the SEIs, the bulk sample (lithium-metal anode), the "native" SEI (decomposition products generated from electrolyte and atmosphere exposure with the lithium metal), the inner SEI, and the outer SEI. The thickness of these layers was determined by using characteristic peaks from each region. A visual depiction of each depth profile and the representative peaks from each region are shown in **Figure 5**a.

In this study, SEI depth is approximated based on the sputtering depth/time required to probe through the majority of the inner and outer SEI species. Using the parameters listed in the Experimental Section, the sputtering time is directly proportional to the sputtering depth, where 1 s of sputtering time equals a
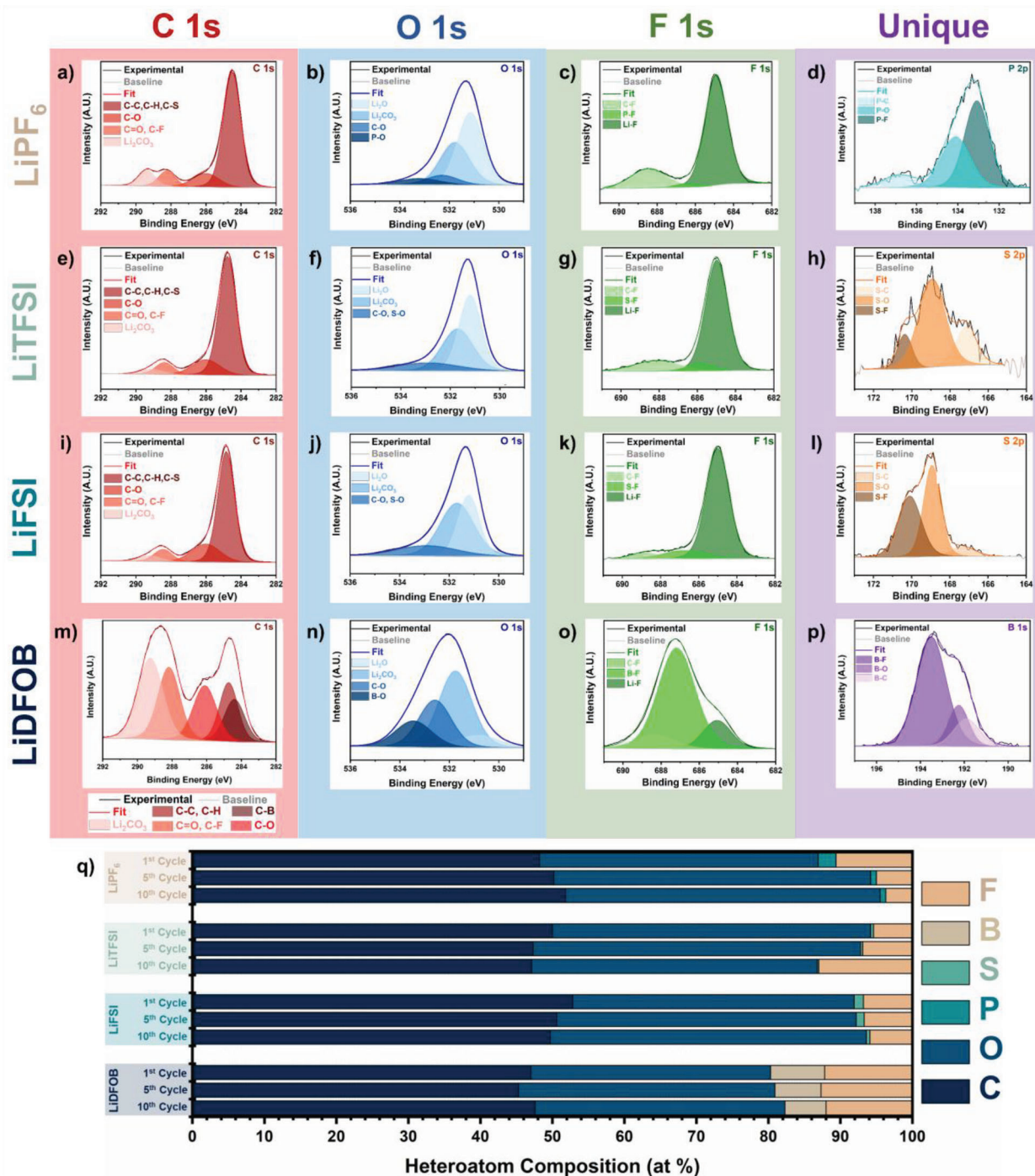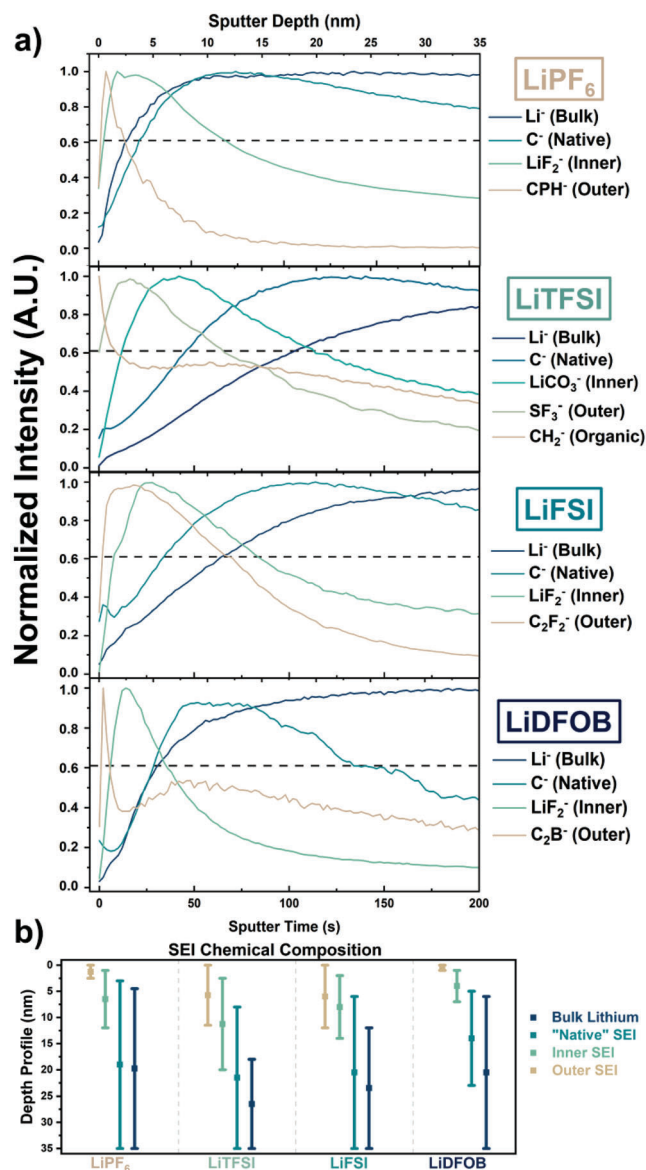
Figure 4. a–p) High-resolution XPS scans of the C 1s (a,e,i,m), O 1s (b,f,j,n), F 1s (c,g,k,o), P 2p (d), S 2p (h,l), and B 1s (p), respectively, of the various electrolyte derived SEI after the 1st cycle. Region scans of the LiPF$_6$, LiTFSI, LiFSI, and LiDFOB derived SEI are shown in (a–d), (e–h), (i–l), and (m–p), respectively. q) Atomic quantification of the heteroatoms (excluding Li) present in the SEI and their composition changes throughout ten cycles at 1 mA cm^{-2} to a capacity of 1 mAh cm^{-2}.

sputtering depth of 0.17 nm. We employed a cut-off value of 0.61 for the normalized intensity for our analyses. This value corresponds to one standard deviation in a normalized Gaussian distribution, thereby allowing this parameter to denote where a majority ($\approx$68.2%) of the respective species is located in the depth

profile of the samples. These results indicate that the LiPF$_6$, LiTFSI, LiFSI, and LiDFOB samples have an SEI thickness of 12, 20, 14, and 7 nm, respectively (Table S3, Supporting Information). Figure 5b summarizes the spatiochemical regions where the outer, inner, and native SEI components appear.
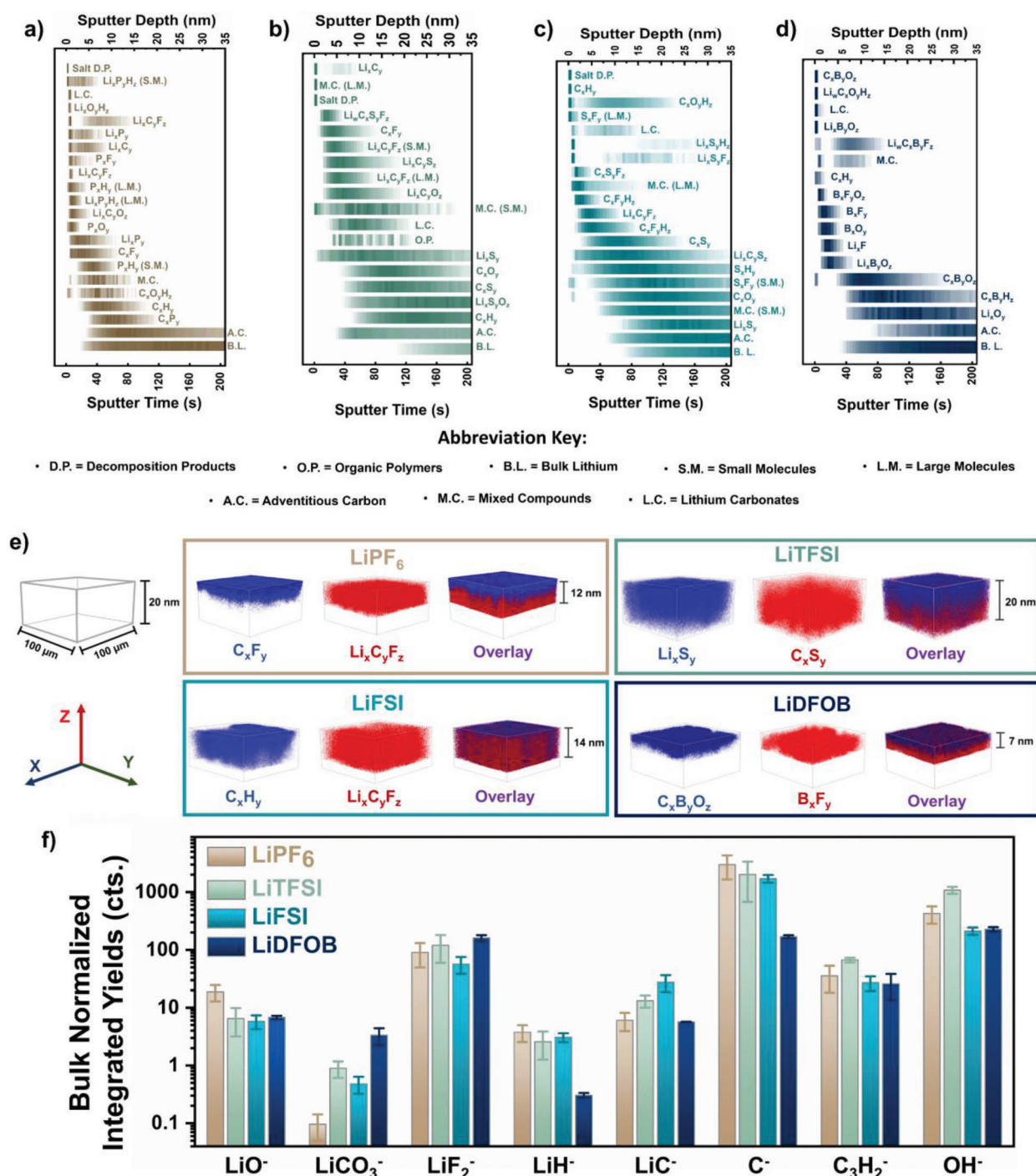
Figure 5. a) ToF-SIMS depth profiles of the various THF-mix derived SEIs after 10 cycles. Representative peaks of ions from the bulk sample, "native" SEI, inner SEI, and outer SEI are depicted to highlight the regions and thickness of the interphase layer. b) Comparison of the spatial composition between each depth profile.

tion being found at similar sputtering depths. However, further studies examining the reaction timescales and pathways for SEI formation/electrolyte decomposition are required to validate this hypothesis.

The heat maps in Figure 6a–d portray the chemical composition of the various SEIs across the length of the SEI (z). To provide insight into the homogeneity of the SEIs from an areal perspective (x,y), maps of the spatial chemical composition for each electrode are shown in Figures S37–S40 in the Supporting Information. For each sample, 2D heat maps of the signal from characteristic ions from the outer SEI, inner SEI, "native" SEI, and bulk components were created at multiple discrete "slices" of sputtering depth (i.e., SEI thickness) to visualize the compositional uniformity across the entire SEI. Areal heat maps of chemical uniformity for the LiPF$_6$ (Figure S37, Supporting Information), LiTFSI (Figure S38, Supporting Information), LiFSI (Figure S39, Supporting Information), and LiDFOB (Figure S40, Supporting Information) electrodes are displayed in the Supporting Information and highlight that electrolyte choice strongly influences the deposition morphology, chemical uniformity, and spatial heterogeneity of the SEI. For example, while lithium was successfully deposited from the LiPF$_6$ electrolyte over the entire electrode area, the spatial distribution of SEI composition was extremely heterogeneous and induced electrodeposition of high surface area structures (Figure S37, Supporting Information). It should be noted that the ultrahigh surface area morphology of the lithium dendrites on the surface may result in the chemical mapping being unable to resolve the intricacies of the topography of the LiPF$_6$ electrode. A similar trend is noted in the LiTFSI (Figure S38, Supporting Information) electrode, demonstrating heterogeneous chemical distribution and depicting a non-uniform lithium plating morphology. Interestingly, the same result is noted in the chemical composition of the electrode cycled in LiFSI (Figure S39, Supporting Information), demonstrating both chemical and lithium nonuniformity. While the LiFSI sample does not exhibit the severe chemical irregularity like LiPF$_6$ nor the severe dendritic growth of LiTFSI, ToF-SIMS mapping of this electrode suggests it suffers from both issues, albeit to a lesser extent than the other electrolytes. In contrast to all the other electrolytes, the high-performing LiDFOB electrolyte system exhibits a relatively flat lithium deposition morphology with only minor spatial heterogeneity of inner and outer SEI species (Figure S40, Supporting Information). To aid in visualizing the chemical composition of these electrolyte-derived SEIs, 3D renderings of these samples were created (Figure 6e).

High-resolution images of the LiPF$_6$ (Figure S41, Supporting Information), LiTFSI (Figure S42, Supporting Information), LIFSI (Figure S43, Supporting Information), and LiDFOB (Figure S44, Supporting Information) provide a visualization of the dendrite morphology, lithium uniformity, and chemical heterogeneity on the surface of the electrode. These images show analogous results to those depicted in the SEM imaging and ToF-SIMS chemical mapping, further elucidating the severity of the chemical heterogeneity of the electrode cycled in the LiPF$_6$ electrolyte. Chemical mapping of representative inorganic (LiF$^-$) and organic (CP$^-$) species highlights the chemical nonuniformity in the depth profile of the anode (Figure S41a,b, Supporting Information).

Combining species identification with hierarchical clustering enabled a noteworthy observation: within a given SEI, species with similar chemical compositions/functionalities also displayed similar depth profiles. As shown in **Figure 6**a–d, this clustering analysis enabled the production of detailed heat maps of the concentration depth profiles of different clustered species, where the color intensity correlates to the normalized value of ion intensity as a function of sputtering depth for representative ion species. One possible hypothesis for this trend is that decomposition products with similar chemical composition will likely follow analogous reaction pathways and have comparable reaction timescales. This results in species of similar chemical composi-

ADVANCED
SCIENCE NEWS
www.advancedsciencenews.com

ADVANCED
MATERIALS
www.advmat.de

Figure 6. Heat maps demonstrating the spatial location of the various chemical species found in the SEI derived from the $LiPF_6$ (a), LiTFSI (b), LiFSI (c), and LiDFOB (d) electrolytes, respectively. e) 3D reconstruction of the various electrolyte-derived SEIs represented by a species found in the outer and inner SEI, respectively, alongside a visualization of these species overlaid. f) Compositional differences in the various SEIs calculated by using the integrated yield of various ion signals normalized to the bulk Li^- signal.

While these analyses depict a comprehensive view of the chemical depth profile of the various electrolyte-derived SEIs, they do not offer information about the concentration of these species. Employing bulk lithium metal as an internal standard, information about the relative concentration of the ions in each sample can be obtained.

can be obtained. This is done by integrating the raw intensity of a respective ion in the region where it is most abundant (region where normalized intensity > 0.61), then dividing this by the raw maximum intensity of the lithium (Li^-) signal. This provides a technique capable of comparing the compositional differences

**ADVANCED
SCIENCE NEWS**

www.advancedsciencenews.com

**ADVANCED
MATERIALS**

www.advmat.de

of shared species between the four samples. Figure 6f depicts the differences in concentrations of various important species that all four SEIs share. The results of this technique demonstrate good alignment with the findings revealed by other analyses. Mirrored in the high-resolution region XPS scans, the $LiPF_6$ sample depicts the highest concentration of Li_2O (LiO^-), and the LiDOFB sample contains the highest concentration of Li_2CO_3 ($LiCO_3^-$). Additionally, the LiF (LiF_2^-) concentrations mimic the XPS atomic quantification of fluorine content within the samples (LiDFOB > LiTFSI > $LiPF_6$ > LiFSI). Ions $C_3H_2^-$ and OH^- were chosen to represent the components formed primarily from solvent (THF and m-THF). The concentration of these ions mirrors the thickness of the SEIs derived from the ToF-SIMS sputtering depth (SEI thickness: LiTFSI > LiFSI > $LiPF_6$ > LiDFOB).

In addition to the information obtained about relative concentrations, this technique can also probe the samples' chemical uniformity. Recent studies by Xu et al. and Wang et al. have discussed how SEI and electrode homogeneity is vital for stable electrodeposition of Li and can have significant implications on the long-term performance of a system.[49,50] As demonstrated by these works and the other analysis we conducted, ToF-SIMS is a useful technique for exploring the homogeneity of a sample. Unfortunately, imaging and 3D reconstructions do not provide quantifiable information about the degree of homogeneity in the sample. To remedy this, we have utilized statistical analysis on the integrated yields of the depth profiles to obtain numerical metrics for heterogeneity within the sample. This is done by taking depth profiles in three separate locations on the metal anode of each sample, then conducting statistical analysis on the obtained integrated yields of each species to obtain a relative standard deviation spatial chemical composition of each SEI. This acts as a metric to measure the degree of chemical heterogeneity within the SEI. Figure 6f depicts the compositional differences between various relevant ions in each SEI. Each sample's average relative standard deviation (RSD) is as follows; $LiPF_6$ = 39.86%, LiTFSI = 37.14%, LiFSI = 25.04%, and LiDFOB = 16.22%. As the high-resolution ToF-SIMS imaging suggests, the LiPF6 and LiTFSI-derived SEI demonstrate the highest heterogeneity; meanwhile, the LiDFOB sample has the most uniform chemical composition.

2.6. Molecular Dynamic (MD) Simulations

Molecular dynamics was run for the 1.14 m simulation cells of each electrolyte (Figure S45, Supporting Information) to determine the Li^+ environment. Radial distribution functions (RDFs) centered around the Li^+, shown in **Figure 7**, were utilized to determine the coordination number of the anions through the presence of the unique atoms within the anion (P, N, and B). Insets within Figure 7a–d highlight the coordination motifs that are attributed to specific features in the RDF. These coordination motifs' enhanced views and the distance between the Li^+ and the respective heteroatom are shown in Figures S46–S49 (Supporting Information) for $LiPF_6$, LiTFSI, LiFSI, and LiDFOB, respectively. The $LiPF_6$ electrolyte (Figure 7a) depicts a unique solvation shell with only two solvation motifs (1a and 2a). This electrolyte has the lowest number of anions in the lithium ions' solvation shells and shows minimal clustering in the simulation. The LiTFSI electrolyte (Figure 7b) also demonstrates limited coordination motifs
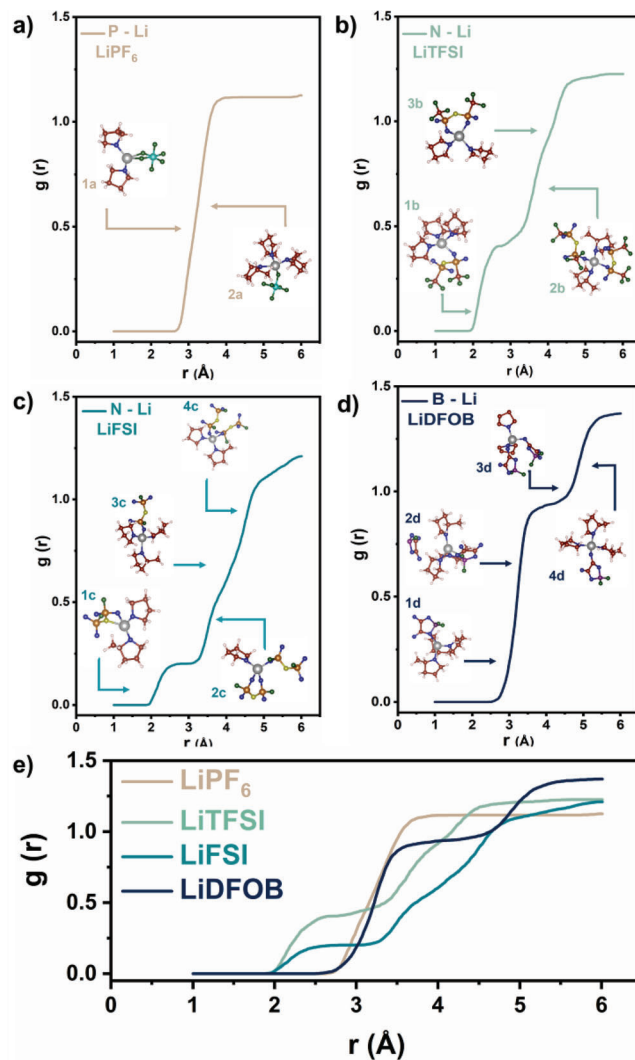
Figure 7. a–d) Radial distribution functions (RDFs) between the Li^+ and the unique atom of the anions (P, S, B, respectively), alongside the relevant solvation motif for the $LiPF_6$, LiTFSI, LiFSI, and LiDFOB electrolytes, respectively. e) Comparison of the RDF for all the electrolytes.

(1b, 2b, and 3b), but the anion has several multicoordination (2b and 3b) motifs that lead to it having the second highest anionic coordination number. The multiple coordination sites in the anion allow the molecule to branch between multiple lithium-ions, thus enabling significant clustering within the electrolyte (3b). The LiFSI electrolyte (Figure 7c) offers a diverse set of coordination motifs (1c, 2c, 3c, and 4c) but has the second lowest coordination number. LiFSI shares structural similarities to LiTFSI that enable the anion to branch between multiple lithium-ions (2c and 3c), showing higher clustering than the $LiPF_6$ system but lower clustering than LiTFSI. The LiDFOB electrolyte (Figure 7d) depicts the highest anionic coordination number and a variety of coordination motifs (1c, 2c, 3c, and 4c). The four oxygen atoms in LiDFOB act as viable coordination sites and provide significant degrees of freedom for the anions to coordinate with Li^+. These coordination sites allow LiDFOB molecules to coordinate between multiple lithium-ions (1d, 3d, and 4d), thus yielding an

ADVANCED
SCIENCE NEWS

www.advancedsciencenews.com

ADVANCED
MATERIALS

www.advmat.de

electrolyte with a high amount of clustering. These results suggest that the anionic coordination of the electrolytes follows the trend of LiPF$_6$ < LiFSI < LiTFSI < LiDFOB (Figure 7e). The coordination environments of the lithium-ions in each of these electrolytes were also quantified to better elucidate their solvation, as shown in Figure S50 in the Supporting Information. All electrolytes (except LiFSI) show a higher population of m-THF coordinated with the lithium-ions, indicating that m-THF may have a higher binding affinity than THF (Figure S50a, Supporting Information). Comparing the solvation motifs (Figure S51, Supporting Information) highlights the weakly solvating nature of the THF-mix solvent system, with all the electrolytes primarily consisting of contact-ion pairs (CIP) and aggregates (AGG) solvation motifs. The LiFSI provides the least favorable solvation structure with 10%, 70%, and 20% of its lithium-ions in solvent-separated ion-pairs, CIPs, and AGG, respectively. Meanwhile, LiPF$_6$ has 80% and 20% of its lithium-ions in CIPs and AGGs, respectively. The LiTFSI and LiDFOB electrolytes demonstrate desirable solvation behavior, with 60% and 40% of the lithium-ions found in a CIP and AGG solvation, respectively. The high concentrations of AGG and CIP structures in the LiDFOB electrolyte may be due to the synergistic properties of LIDFOB and THF. LiDFOB has a very low dissociation constant in an inorganic solvent, alongside THF's weakly solvating nature, causes exceptionally high amounts of anion–cation pairing in the inner solvation shell even at low salt concentrations.[51]

To corroborate these results, Li$^+$ binding energies were calculated for each electrolyte component (Table S4, Supporting Information) and their potential binding modes (Figure S52, Supporting Information). Comparing the BE of all the electrolyte components depicts a general trend where THF > m-THF > DFOB$^-$ > PF$_6^-$ > FSI$^-$ > TFSI$^-$. This result supports our hypothesis of the weakly solvating nature of the THF and m-THF solvents, as these electrolytes have a comparatively lower binding affinity to Li$^+$ versus the anions. Additionally, the higher binding energy of THF elucidates why the m-THF solvent preferentially coordinates with Li$^+$. PF$_6^-$ demonstrates the second highest binding energy of all the anions and exemplifies why the electrolyte shows low anionic coordination. Interestingly, DFOB$^-$ has the highest BE of the anions, even though it demonstrated high-level anionic coordination to Li$^+$. This is likely because DFOB$^-$ can only coordinate to one site per Li$^+$ due to the sterics of the molecule. Comparing the one coordination site BE of each anion, a different trend is revealed, where PF$_6^-$ > FSI$^-$ > DFOB$^-$ > TFSI$^-$. Demonstrating that DFOB$^-$ has the second lowest BE for anions, only coordinating once to Li$^+$, suggests that DFOB- is less enthalpically favored to bind to Li$^+$ than the other anions. However, DFOB$^-$ may be more entropically favored, as supported by the coordination behavior of DFOB$^-$ which has a diverse set of binding motifs, more coordination sites per molecule than the other anions, and can readily coordinate with multiple lithium-ions. In addition, TFSI$^-$ has the lowest BE for both one and two site coordination, which aligns with the other MD results, depicting the highest anionic coordination in the Li$^+$ solvation shell.

The ionic diffusivity of the electrolytes was calculated with the MD simulations by using the total trajectory of the lithium-ions during the simulation time, the methodology of which is fully detailed in the Supporting Information. The results suggest that the ionic diffusivities followed the trend of LiPF$_6$ < LiDFOB <
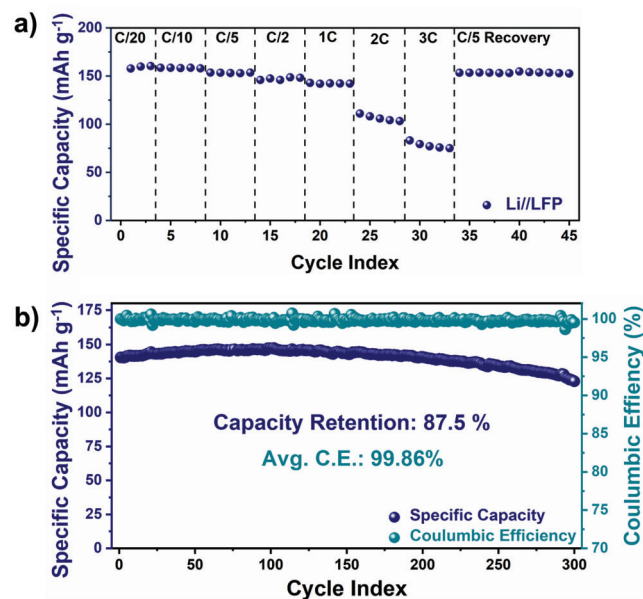
Figure 8. Electrochemical performance testing of Li//LFP and cells employing a 1.15 M LiDFOB electrolyte. a) Variable rate performance testing conducted from C/20 to 5C rates. b) Long-term stability testing conducted at a rate of C/2.

LiFSI < LiTFSI (Table S5, Supporting Information). These results demonstrate similar trends to the previously conducted viscosity and ionic conductivity measurements, depicting that LiDFOB has the highest ionic mobility. Furthermore, these results also suggest that the LiFSI and LiTFSI electrolytes have comparable ionic mobility, with the LiTFSI electrolyte having slightly higher ionic conductivity and diffusivity than LiFSI. The calculated ionic diffusivity of the LiPF$_6$ electrolyte was lower than anticipated; however, these simulations do not induce an applied potential on the system. Therefore, differences in charge carrier mobility and density could be the origin of the differences between ionic conductivity and diffusivity.

2.7. Full Cell Compatibility Testing

These electrolytes all demonstrated similar oxidative stability, achieving an upper voltage of ≈4.1 V, in agreement with other THF and THF-mix electrolyte studies.[30,32,33] The LiDFOB electrolyte system was further tested for practical lithium-ion chemistries using a Li//LFP full-cell configuration due to its superb performance. Variable rate performance testing and long-term stability cycling of cathodes with practical mass loadings (avg. 7.13 mg cm^{-2}, 1.21 mAh cm^{-2}) were employed for evaluation (**Figure 8**). The complete physical properties of the LFP electrodes can be found in Table S6 in the Supporting Information. Variable rate cycling (Figure 8a) using the LiDFOB electrolyte provided noteworthy results, delivering an initial capacity of 160 mAh g^{-1} (≈1.14 mAh cm^{-2}) and exceptional capacity retention at both fast (1C, 139 mAh g^{-1}, ≈0.99 mAh cm^{-2}) and extreme (3C, 77 mAh g^{-1}, ≈0.55 mAh cm^{-2}) cycling conditions. Charge–discharge curves of the various cycling rates can be found in Figure S53 in the Supporting Information.

**ADVANCED
SCIENCE NEWS**

www.advancedsciencenews.com

**ADVANCED
MATERIALS**

www.advmat.de

Additionally, tabulated values of the average specific capacities and capacity retention at each cycling rate can be found in Table S7 in the Supporting Information. These results demonstrate that the LiDFOB system stabilizes the lithium anode under high current density applications and provides an ionically conductive medium capable of fast Li^+ transport even with practical cathode chemistries and loadings. Long-term stability testing (Figure 8b) was employed to test the longevity of the electrolyte and its ability to minimize dendrites in full cells. These flooded cells provided stable energy storage for over 300 cycles, maintaining a capacity retention of 87.5%, an average Coulombic efficiency of 99.86% with an initial capacity of 139 mAh g_{LFP}^{-1} ($\approx$0.99 mAh cm^{-2}). The LiDFOB THF-mix system provides competitive performance to other next-generation lithium-metal battery electrolytes (Table S10, Supporting Information, demonstrating excellent Coulombic efficiency and rate performance. Additional investigation of the charge–discharge curves (Figure S54, Supporting Information) supported these results, showing the minor change in the profile of the curves and minimal voltage hysteresis throughout cycling.

3. Discussion

Combining all results of the employed analytical and electrochemical techniques (i.e., SEM, ToF-SIMS, XPS, EIS, galvanostatic cycling) allows for: (1) a comprehensive examination of the composition and properties of the various SEIs and (2) their influence on electrochemistry and performance of the lithium-metal anodes. To aid in this understanding, the physical (bulk, shear, and Young's modulus) and chemical (ionic conductivity, bandgap, electronic conductivity) properties of notable species detected by XPS and ToF-SIMS will be discussed and tabulated in Table S8 in the Supporting Information. Previous studies have shown that the ratio of bulk (B) to shear (G) modulus (i.e., B/G ratio) can be used to approximate the ductility of an SEI component, with $B/G < 1.75$ showing poor flexibility, $1.75 < B/G < 2.00$ showing moderate ductility, and $B/G > 2.00$ showing great flexibility.[52] It should be noted that while the properties of an individual SEI component likely will not dictate the overall properties of the interphase, the various components' synergistic attributes likely influence the system's cumulative electrochemical properties.

A cursory glance at the characterization results of the $LiPF_6$ electrolyte system suggests it could provide respectable electrochemical performance, as the electrolyte demonstrates relatively low viscosity and high ionic conductivity and results in an SEI with a large proportion of anion-derived inorganics ($\approx$13.2 at% of nonlithium species via XPS) (Table S1, Supporting Information). However, this system surprisingly demonstrated poor electrochemical performance at high current densities (Figure 2b), exhibiting electrochemical instability (e.g., fluctuating overpotentials and formation of dead lithium), short cycle-life, continual SEI growth, and the deposition of dendrite structures with large surface areas. The observed instability is likely attributed to the weak mechanical properties and nonspatially uniform chemical composition of the PF_6^--derived SEI. ToF-SIMS (Figure 6a) and XPS (Figure 4a–d) revealed an abundance of phosphorus oxides and oligomeric polyethers that exhibit low mechanical strength (e.g., P_2O_5 ($B = 12$ GPa, $G = 5$ GPa)[53] and PEO ($B = 2.5$ GPa,

$G = 0.9$ GPa)[52,54]). Furthermore, XPS region scans suggest that the $LiPF_6$ electrolyte decomposition reactions resulted in the preferential formation of Li_2O over Li_2CO_3 (Figure 4a,b; Figures S15 and S16, Supporting Information). This is supported by the compositional analysis (Figure 6f), which shows that the $LiPF_6$ contains the lowest amount of Li_2CO_3 and the highest amount of Li_2O out of all the samples. Where Li_2O provides only moderate ductility and is extremely ionically insulating ($B = 81$ GPa, $G = 45.6$ GPa, $B/G = 1.76$, 1.0×10^{-12} S cm^{-1}), Li_2CO_3 ($B = 55$ GPa, $G = 27$, $B/G = 2.04$, $\approx 1 \times 10^{-6}$ S cm^{-1}) is an SEI component that provides similar mechanical strength but demonstrates higher elasticity and ionic conductivity than Li_2O.[55,56,57] While ionic conduction typically occurs through the grain boundary of the SEI components, generating a Li_2O-rich (and Li_2CO_3-poor) SEIs could limit ionic transport or induce excessive ionic resistance through the interphase. Furthermore, this composition provides mechanically unstable passivation during expansion/contraction upon lithium plating/stripping.

Interestingly, the $LiPF_6$ electrolyte generates a relatively thin SEI, with the bulk of lithium reaching within $\approx$12 nm (Figure 5b), suggesting the electrolyte generates highly electronically resistive products that quickly passivate electron transfer between the electrode and electrolyte. While the SEI is too thick to be probed completely by XPS (Figures S15–S18, Supporting Information), conducting this analysis throughout the anode's cycle life elucidates how the chemical composition shifts throughout the SEI growth process. As noted from the change in chemical composition from the electrode's 1st cycle SEI to the 10th cycle (Table S1, Supporting Information), the SEI is progressively getting more organic as it cycles. We hypothesize that the $LiPF_6$ is chemically reactive and forms a highly inorganic passivation layer before cycling; however, its weak properties require additional passivation of the electrode surface as mechanical stress of lithium plating and stripping cause the SEI to fracture. The low anionic coordination in the Li^+ solvation shell (Figure 7a) results in the growth of organic decomposition products during electrochemical cycling. Thereby suggesting the compositional shift is likely perpetuated by the synergist effect of: (1) low anion presence in the Li^+ solvation shell leading to less migration of anions to the electrode surface during cycling and (2) preferential chemical decomposition of the salt before cycling leads to a depletion of inorganic components for future SEI passivation. These newly formed organic species also provide poor mechanical stability, perpetuating additional SEI formation, lithium growth instability, and the cells' inevitable failure.

Investigating the holistic composition of the $LiPF_6$ SEI through ToF-SIMS reveals another interphase issue: its chemical composition is incredibly complex and heterogeneous. The ToF-SIMS spectra of the $LiPF_6$-derived SEI identified considerably more unique ions (138) than the other electrolytes, suggesting that the $LiPF_6$ electrolyte results in a relatively more diverse range of electrolyte decomposition products. ToF-SIMS compositional analysis (Figure 6f) elucidates the heterogeneous nature of the SEI (39.86% avg. RSD). In addition, these diverse species were deposited with extreme spatial heterogeneity, as demonstrated by chemical heat maps of the SEI (Figures S37 and S41, Supporting Information). Such a heterogeneous SEI likely disrupted uniformity in ionic flux during stripping/plating, inducing hotspots for the growth of high surface area dendrites as depicted in the

**ADVANCED
SCIENCE NEWS**

www.advancedsciencenews.com

**ADVANCED
MATERIALS**

www.advmat.de

electrode's postmortem SEM images (Figure 3a,e,i). The high surface area morphology of the lithium dendrite formations also perpetuates the electrochemical instability of the system, being more likely to fracture and form dead lithium during cycling. This, alongside SEI's poor mechanical properties, requires continual passivation during the cycling process as dendrites break and the SEI fractures. The effects of these factors are exhibited by the poor electrochemical performance of the $LiPF_6$ electrolyte; however, these tests were done using flooded cells. In practical, electrolyte-limited settings, we expect the cycle life and performance to be further diminished.

The LiTFSI electrolyte exhibited significantly enhanced cycling stability compared to the $LiPF_6$ system at large current densities but provided overall suboptimal electrochemical performance with relatively high overpotentials. The chemical composition (Figure 4q) of the LiTFSI-derived SEI depicts the lowest 1st cycle inorganic composition (5.8 at%) of all the THF-mix electrolytes, yet the inorganic composition of the SEI grows throughout the cycling process (7.3 at% at 5th cycle, 13.2 at% at 10th cycle). It should be noted that while XPS does not provide quantitative information about the bulk of the LiTFSI-derived SEI due to its thickness (Figure 5b, ≈20 nm), it includes information about the change of chemical composition on the surface of the SEI. The drastic change in the surface composition of the SEI throughout cycling suggests that the initial interphase is unstable and requires supplementary passivation. Additionally, it insinuates that electrochemical decomposition reactions (induced by an applied electrochemical potential) favor the breakdown of the anions over the solvent, whereas the chemical reactions (spontaneous reactions) preferentially decompose the solvent in the LiTFSI electrolyte.

This is further supported by the unique composition of the LiTFSI-derived SEI revealed by ToF-SIMS, where the SEI consists of a thin exterior organic layer, followed by an outer and an inner inorganic layer (Figure 5a). These two inorganic layers are likely derived from the different species created from electrochemical and chemical reactions, respectively. The inner inorganic layer likely forms during the rest period of the cell but does not provide sufficient stability/passivation and requires additional SEI formation, whereas the outer layer is formed during the cycling of the cell. MD simulations of the LiTFSI electrolyte demonstrate that the $TFSI^-$ is highly coordinated to Li^+ (Figure 7b); this results in a high concentration of anions on the Li surface upon voltage polarization in the cell and increased likelihood of anion decomposition during this process. Corroborated by the XPS quantitation (Figure 4q), the decomposition products formed through cycling preferentially break down the anion resulting in a significant increase in F concentration. This is further supported by the 3D rendering of the interphase showing that the LiTFSI-derived SEI depicts less distinct, more gradient-like layers in its chemical composition (Figure 6e). This unique growth pattern and excessive electrolyte consumption provide an unfavorable platform for long-term performance and electrolyte-limited conditions. The initial organic-rich SEI is likely mechanically unstable and chemically heterogeneous (Figure 6f, RSD = 37.14%; Figure S38, Supporting Information), thus generating nonuniform lithium deposition (Figure S12b, Supporting Information) and excessive dendrite formation (Figure 3b). The low Young's modulus (E) of the organic constituents (generally <1 GPa) pro-

vides poor physiochemical stability of the initial SEI;[25,52] however, the formation of the electrochemical decomposition products generates an inorganic-rich exterior which assists in the passivation and cycling stability of the electrode. As postmortem imaging (Figure 3f,j) revealed, the SEI compositional change causes a shift in the deposition morphology, becoming more uniform and creating dendrites with lower surface area morphologies. Yet, the multifaceted SEI growth mechanism forms a thick (≈20 nm, Figure 5b), chemically heterogenous passivation layer, which increases the difficulty of ion mobility and induces large overpotentials to the plating/stripping processes (Figure 2).

This investigation of LiTFSI in THF-mix electrolytes demonstrates the importance of the SEI formed before the first-cycle (i.e., chemically vs electrochemically-induced SEI) on the sustained lithium deposition morphology and achievable long-term performance and stability of Li anodes. The self-perpetuating nature of dendritic electrodeposition[3,7] means that Li dendrites seeded as early as the first cycle could eventually lead to cell failure.[58] This aligns with the results of the chemical maps from ToF-SIMS (Figures S38 and S42, Supporting Information), which depict lithium heterogeneously deposited on the electrode. As such, the LiTFSI system demonstrates a relatively short cycle life under both low (Figure 2a, ≈625 h) and high (Figure 2b, ≈250 h) current density conditions.

The LiFSI electrolyte generated an SEI containing decomposition products similar to those observed in the LiTFSI system (Figure 6c). Despite similarities in their chemical makeup, the distinct differences in the SEI composition, morphology, and chemical uniformity strongly impacted the observed cycling stability in the LiFSI electrolyte compared to the LiTFSI electrolyte. The LiFSI-derived SEI demonstrates only a moderate inorganic chemical composition (8.0 at%) yet contains a significantly higher concentration of S (1.3 at%) than the LiTFSI-derived SEI (Figure 4q), exhibiting significantly more S–O, Li–S, and S–F containing compounds (Figure 4l). SEIs comprised of Li_xS_y compounds often have high physical properties and high ionic conductivities (e.g., LiS, B = 40 GPa, with a small Li^+ conduction barrier of 0.39 eV).[25,59] LiFSI produced an SEI with more Li_2CO_3 (Figure 4i) and C–F fluoride species (Figure 4k). Previous works implicate that the preferential formation of inorganic fluoride functionalities (e.g., Li–F, S–F, etc.)—instead of C–F species—is favorable stable lithium plating/stripping.[31] ToF-SIMS chemical mapping representation of the depth profile (Figure S39, Supporting Information), the surface mapping (Figure S43, Supporting Information), and compositional analysis (Figure 6f, avg. RSD = 25.04%) demonstrate that Li–F species are homogenously dispersed throughout the SEI derived from the LiFSI electrolyte. Compared to either $LiPF_6$ or LiTFSI, the more uniform composition and architecture of the LiFSI-derived SEI exhibited physical and chemical properties that were seemingly both conducive to uniform Li^+-ion flux and mitigation of SEI fracture, enabling homogenous lithium deposition during repeated plating/stripping. Lithium deposition morphology plays a significant role in the overall cell performance, as thin morphologies with high surface area to volume ratios are both more likely (1) to consume Li inventory via SEI formation and generation of dead lithium (i.e., stripping-induced electronic isolation from "live lithium") and (2) to fracture (electronic disconnection, mechanically dead lithium, etc.) dendrite formations.

**ADVANCED
SCIENCE NEWS**

www.advancedsciencenews.com

**ADVANCED
MATERIALS**

www.advmat.de

For the LiFSI electrolyte system, postmortem SEM imaging of deposition from the LiFSI electrolyte (Figure 3c) revealed a low surface area and cluster-like morphology plated uniformly across the electrode after the 1st cycle. After subsequent cycling of the electrode, the morphology transitioned toward denser, "sheet-like" structures (Figure 3g,k), which promoted stability throughout the cell's life cycle, with no noticeable spikes or fluctuations observed in the voltage excursions until critical device failure. This stability is highlighted by the XPS quantification (Tables S1 and S2, Supporting Information) and region scans (Figures S15–S17, Supporting Information), which demonstrate little to no change throughout cycling. While providing stable cycling, the low ionic conductivity (5.82 mS cm^{-1}) and diffusivity (3.03 × 10^{-5} m^2 s^{-1}) of the electrolyte and relatively thick SEI layer (≈14 nm) contribute to the moderately-high overpotentials for the plating/stripping process (≈20 and 45 mV at 0.5 and 1.0 mA cm^{-2}, respectively) before eventual cell failure through dendritic shorting (Figure 2).

Comparing the results of the LiTFSI and LiFSI systems further emphasizes the importance of the properties not only of an electrolyte but also of the resulting SEIs they create. The LiTFSI and LiFSI electrolytes have an analogous chemical composition and physical properties, such as their viscosities (1.31 vs 1.29 cP) and ionic conductivities (6.72 vs 5.82 mS cm^{-1}). Furthermore, these electrolytes shared similar electrochemical properties, such as their nearly identical impedance spectra (Figure 1d), differential relaxation times (Figure 1e), and initial over potentials under high current density conditions (Figure 2b). These electrolytes generated very similar decomposition products, sharing over 85% of the same products (Figure S56b, Supporting Information) in their mass spectra. However, the increased concentration of inorganic fluorides and the chemical uniformity of their resulting SEI drastically influenced their long-term stability under both low and high current density conditions.

Electrochemical testing of the LiDFOB system provided astounding results, demonstrating low overpotentials and extensive cycle life (Figure 2) under both low (≈3200 h) and high current density (≈1700 h) conditions. We attribute these exceptional properties to the desirable physical properties of the electrolyte and the resulting SEI chemical composition. The LiDFOB electrolyte touted the lowest viscosity (1.1 mPa s), highest diffusivity (5.52 × 10^{-5} m^2 s^{-1}), and highest ionic conductivity (16.1 mS cm^{-1}) of the electrolytes tested in this study. Additionally, the SEI exhibited remarkably high inorganic composition (19.6 at%) (Table S1, Supporting Information). The exceptionally high inorganic composition can be partially attributed to the solvation structure of the LiDFOB electrolyte. The synergistic nature of the weakly dissociated LiDFOB salt and the weakly solvating THF mixture creates an electrolyte with high anion–cation pairing in the solvation shell. This electrolyte demonstrates the highest anionic coordination number of all the electrolytes (Figure 7e) and has the highest number of anions per Li$^+$ in the primary solvation shell (Figure S50, Supporting Information). The unique solvation enhances the solvent's reductive stability and promotes preferential decomposition of the salt, resulting in an inorganically rich SEI.

Investigation of the specific species found in the SEI reveals a diverse set of compounds that offer unique benefits to the chemical and physical properties of the SEI, containing species that offer the mechanical, electronically insulating, and ionically conductive properties for an optimal SEI. The LiDFOB-derived SEI has several mechanically robust materials, such as Li$_2$CO$_3$ (Figure 4m) and LiF (Figure 4o). Notably, the SEI contains considerably more Li$_2$CO$_3$ than any of the other SEIs analyzed here, as noted by the C 1s region (Figure 4m), where the ratio of Li$_2$CO$_3$: C–C, C–H functionalities are nearly 1:1. The high concentrations of Li$_2$CO$_3$ and LiF is further corroborated by the ToF-SIMS compositional analysis (Figure 6f), depicting the highest concentration of these compounds out of all the THF-mix electrolyte-derived SEIs. As previously mentioned, Li$_2$CO$_3$ and LiF blend mechanically tough and robustly ductile properties to promote a stable SEI. The LiF component also acts as an electronic insulator, promoting thinner SEI formation. Recently, LiH has been shown to impact the electrochemical stability of lithium-metal anodes as it is prone to induce hydrogen evolution reactions.[60,61] A significantly lower concentration of LiH was detected in the LiDFOB SEI (Figure 6f) compared to all of the other systems. The LiDFOB-derived SEI has several beneficial species that were also identified in the other SEIs discussed in this manuscript; however, the LiDFOB salt system also has numerous unique B-derived species (Figures 4p and 6d), such as LiBO$_2$, B$_x$O$_y$, and BF$_x$, in its SEI. LiBO$_2$ is a notable species due to its beneficial mechanical, electronic, and ionic properties. LiBO$_2$ is a mechanically robust and flexible component of the SEI (B = 60 GPa, G = 29 GPa, B/G = 2.07), promotes efficient lithium-ion mobility with its low activation energy barrier for Li$^+$ ion migration (≈0.22 eV), and provides sufficient electronic insulation due to its large bandgap (theoretical E_g = 6.29).[59,62,63] Boron oxides also provide similar desirable electronic and ionic conductivity properties, with B$_2$O$_3$ having a sizeable bandgap of 6.30 eV and being used as a core component for Li$^+$ conducting ceramics.[64,65] It should be noted that other studies have shown that LiDFOB will react with the ether-based molecules to form crosslinked oligomeric polymers.[66,67] These compounds do not have high mechanical moduli but often demonstrate high ductility and ionic conductivity. Works by Fu et al. have demonstrated that the incorporation of mechanically strong materials in matrices of soft, polymer-like materials with low shear moduli can enable the suppression of dendrite formation and may explain the exceptional long-term stability of the system.[68]

Experimental results and postmortem analysis of the LiDFOB system denote the synergistic role of species, such as the boron oxides, Li$_2$CO$_3$, LiF, and oligomeric polymers, in the system's overall performance. As determined by ToF-SIMs, the LiDFOB system generates an extremely thin SEI even after multiple cycles (≈7 nm, Figure 5b), consisting of two discrete layers: (1) a thin outer layer primarily consisting of organic materials and (2) a thicker inorganic-rich inner SEI. The ideal properties of the overall SEI are a product of the synergistic attributes of its components. These properties promote the formation of a thin, electronically insulating, ionically conductive, and mechanically robust SEI. Furthermore, ToF-SIMS chemical depth profile mapping (Figure S40, Supporting Information), surface mapping (Figure S44, Supporting Information), and compositional analysis (Figure 6f, 16.22% avg RSD) showed that the LiDFOB-derived SEI displayed the most spatially homogeneous chemical composition out of all the investigated THF-mix electrolytes. The chemical uniformity of the system may be a factor in the

discrete decomposition pathways of the LiDFOB electrolyte as the mass spectra of the LiDFOB SEI demonstrated the least number of unique ions (80), potentially suggesting a smaller chemical reaction network of decomposition pathways. Combining the SEI's chemical homogeneity and ionically conductive encourages homogenous Li^+ flux and deposition, creating uniform lithium depositions with extremely low surface areas (Figure 3d). These favorable deposition morphologies, in addition, to the mechanically robust nature of the SEI, encourage stable cycling and minimal changes in the electrode's physical and chemical composition throughout cycling (Figure 3h,l; Table S1, Supporting Information).

The formation of thin, mechanically robust SEIs has been observed in other electrolyte systems employing LiDFOB. In this present study, we attribute the improved performance attained from our system to be due to the THF-mix electrolyte, which encourages anion decomposition and results in a uniform, inorganic-rich SEI. The synergistic properties of the SEI components result in an interphase capable of promoting stable, long-term lithium plating/stripping in lithium-metal batteries. Noting the success of the LiDFOB-based electrolyte in lithium symmetrical cell formats, we investigated this system's compatibility with practical lithium-ion chemistries. LSV of the various THF-mix electrolytes denoted that these electrolytes had an electrochemical stability of ≤ 4.1 V vs Li/Li^+. Therefore, the practicality of the LiDFOB electrolyte was tested using a Li//LFP format. Testing of this system demonstrated that the electrolyte's low viscosity and high ionic conductivity were conducive to high-rate ($\geq$3C) cycling (Figure 8a). Furthermore, long-term testing showed respectable capacity retentions and high Coulombic efficiencies (Figure 8b). A comprehensive comparison of these results with recent literature reports, Table S10 (Supporting Information), provides a transparent view of how the performance of this electrolyte compares to other next-generation electrolytes for lithium-metal batteries.

The investigations of this study have demonstrated how WSEs, such as THF and m-THF, encourage the formation of favorable solvation structures, such as CIP and AGG, even at low concentrations. These electrolytes enable the preferential decomposition of the anion, thereby allowing purposeful anion selection to be used to tune the chemical composition of the resulting SEI. Employing a swath of analytical techniques such as SAXS, SEM, XPS, and ToF-SIMS allowed for a comprehensive investigation of the resulting SEIs and the electrochemical implications of their chemical composition and morphology. This systematic approach to investigating the SEI enabled clear explanations for the possible failure modes of the lithium-metal anodes. The cluster analysis-based workflow for the ToF-SIMS enabled a thorough understanding of these systems, which provided a spatially resolved chemical map of the SEI. This holistic view of the SEI enabled a better understanding of the system and its impact on the anode's electrochemical plating/stripping reactions. Standardizing this cluster analysis-based workflow in LIB systems would accelerate the scientific communities' understanding of the SEI.

4. Conclusions

THF-based electrolyte systems demonstrate superior performance for lithium-metal batteries by generating inorganic-rich SEIs that enable stable, uniform lithium deposition throughout cycling. The unique solvating properties of these THF electrolytes promote the presence of ion aggregates and contact-ion pairs, which enable the preferential decomposition of the salt component of the electrolyte. Employing a breadth of lithium ionic salts, we explore the influence of different electrolyte anions on the resulting SEI in lithium-metal batteries. Advanced chemical analysis combining ToF-SIMS and XPS generates a complete chemical profile of the resulting SEI. Furthermore, through advanced multivariate statistics, hierarchical clustering of the depth profiles obtained from the comprehensive ToF-SIMS analysis enabled spatially resolved chemical mapping of the SEIs. In general, the "salt directing" nature of the tetrahydrofuran-based electrolytes results in SEIs with considerably inorganic-rich chemical compositions for all the Li salts employed. However, specific chemical composition was determined by the anion-derived decomposition products, and our work emphasizes that even inorganic-rich SEIs can promote unstable Li electrodeposition if the chemical composition is spatially heterogeneous. Systematic exploration of the interphases' electrochemical and physical properties further reveals the synergistic influence each decomposition product has on the overall performance and attributes of SEI. Together, excellent ionic, mechanical, and electrical properties of the LiDFOB-derived SEI provided an efficient platform for extremely stable lithium plating/stripping in symmetrical cells ($\approx$1700 h @ 1 mAh cm^{-2}, 1 mA cm^{-2}) and long-term cycling in Li//LFP coin cell battery (300 cycles w/ 87.5% capacity retention). We believe that further efforts in electrolyte engineering can employ lessons learned from these advanced analytical techniques to better stabilize the interphase on lithium anodes for the eventual generation of safe, fast-charging, and energy-dense lithium-metal batteries. Exploration of novel solvents that may offer similar "salt directing" properties, such as tetrahydropyran and lithium salts with favorable decomposition products, could further advance the community's ability to engineer the formation of favorable lithium-metal SEIs. Additionally, our study has demonstrated how an inorganic-rich SEI composition is not sufficient for stable electrochemical performance; SEI composition must enable robust mechanical properties, ionic conductivity, and chemical uniformity for desirable performance. Future work should investigate how electrochemical substrate effects influence SEI formation mechanisms and composition. Anode-free systems employing copper substrates are particularly interesting as eliminating native SEI formation could significantly affect the composition of the resulting SEI and the cell's performance.

This work highlights the importance of both solvent and salt selection in lithium-metal batteries and delineates the analytical power of ToF-SIMS techniques to assist with understanding the intricate chemical composition of the SEIs. Hierarchical clustering and compositional analysis through integrated yields are both techniques not readily employed by the lithium-ion battery community. However, utilizing the hierarchical clustering analysis in this study, a holistic view of the spatiochemical composition of the SEI was able to be established. This provided fundamental insight into the chemical makeup of the interphase and elucidated possible mechanisms of formation. Additionally, calculation and statistical analysis of the integrated yields for various species provided quantitative information about the SEI composition and uniformity. Traditionally, ToF-SIMS provides detection

**ADVANCED
SCIENCE NEWS**

www.advancedsciencenews.com

**ADVANCED
MATERIALS**

www.advmat.de

and qualitative information about the species within the sample, yet through the implementation of this analysis, we obtain relative compositional comparison and measure the degree of chemical uniformity. ToF-SIMS has the potential to provide significant insight into the chemistry and topographical composition of battery systems; unfortunately, the cumbersome amount of data obtained from this technique often limits the full utilization of its capabilities. Standardizing these protocols would help the battery community better understand their systems and provide more comprehensive examinations of their chemistries. We believe these novel ToF-SIMS analyses will be essential to the battery community and enable a more comprehensive understanding of the elusive SEI.

5. Experimental Section

Materials: All chemicals were used without further purification or treatment unless stated otherwise. Lithium hexafluorophosphate (LiPF$_6$, 99.99%), tetrahydrofuran (THF, 99.9%), 2-methyltetrahydrofuran (m-THF, 99%), lithium difluoro(oxalato)borate (>99.9%), lithium bis(trifluoromethane)sulfonimide (LiTFSI, >99.0%), and lithium bis(fluoromethane)sulfonimide (LiFSI, 99.9%) were obtained from Sigma-Aldrich. The Super P conductive additive, polyvinylidene fluoride binder (PVDF, >99.5%), and LFP (carbon coated LiFePO$_4$, D_{range} 1–15 µm, D_{50} 2.5–4.5 µm) were acquired from MTI Corporation. *N*-methyl-2-pyrrolidone (NMP, >99%) was obtained from Tokyo Chemical Industry Co., Ltd. (TCI). 750 µm thick Li foil (99.9%) was purchased from Alfa Aesar. Celgard 2400 microporous monolayer membranes (polypropylene, 25 µm) were generously provided by Celgard.

Electrochemical Analysis: All electrochemical analysis was conducted using 2032 coin-type formats, with the cell parts obtained directly from MTI Corporation. All cells were assembled using a Celgard 2400 polymer membrane and a 1.15 m (≈1 M) electrolyte composed lithium-based salt in tetrahydrofuran (THF)/2-methyltetrahydrofuran (m-THF) (1:1 by volume) solution. The resulting solution compromised of these two solvents will be referred to as THF-mix for the rest of the manuscript. This study investigates the implications of substituting the anion component of lithium salt. The salts investigated in this study were LiDFOB, LiFSI, LiTFSI, and LiPF$_6$. Investigating lithium bis(oxalato), borate was also intended to act as a fluorine-free candidate for this study; unfortunately, its nearly negligible solubility in THF-mix solvents prevented further exploration. An excess of electrolyte (>5 drops) was used to flood the cell and provide sufficient wetting. The flooding of electrolytes was used to minimize the performance effects caused by electrolyte depletion and better highlight the effects SEI composition played on cycling behavior. Li//Li cells were fabricated using 750 µm thickness Li. Circular electrodes were cut using a 0.53 inch die punch. Cycling performance tests were conducted using a multichannel battery test system (BTS4000, Neware). The electrochemical data presented is an average of three identical cells to assure reproducibility. All cycling was conducted using an initial 12 h rest step and a 5 min resting period between each charge and discharge. Electrochemical impedance spectroscopy was performed galvanostatically with a Gamry Interface 1010E potentiostat employing a 0.1–200 000 Hz frequency range and an oscillating current of 10 µA.

Postmortem Analysis: Postmortem analysis was conducted on the cells after the charge step of the *X*th cycle. All postmortem cells were cycled at 1.0 mA cm^{-2} to a capacity of 1.0 mAh cm^{-2}. Cells were transferred into the argon-filled glovebox, and the electrodes were extracted using a TMAX disassembly tool. This enabled the deconstruction of the coin cell without damaging the lithium electrodes or causing an internal short circuit. All electrodes were gently washed using three 0.3 mL aliquots of THF to remove residual electrolyte and lithium salts. Electrodes were then allowed to dry before transport to their respective analysis area using an inert transfer vessel.

Full Cell Electrode Preparation: LFP-based electrodes were fabricated using an NMP-based solvent system and a PVDF binder. The solid composition of the slurries consisted of an 85:10:5 weight ratio of active material: Super P: polymer binder. Slurry solutions were then cast using a doctor blade set to a height of 100 µm. Tabulated results of the electrodes' complete physical properties can be found in the Supporting Information (Table S6, Supporting Information). Slurries were cast onto 12 µm thick aluminum foil at room temperature, and the resulting electrode films were subsequently dried for two hours at 120 °C under ambient pressure to evaporate the majority of the solvent. These films were dried overnight under a vacuum to drive off the remaining solvent. Circular electrodes were punched directly from the electrode films with a TMAX die electrode punch with a diameter of 13 mm for the cathode. This diameter ensured the cathode was entirely eclipsed by the 0.53 in (≈13.5 mm) lithium anode. The thicknesses of the resulting electrodes were measured using an IP65 Digimatic micrometer. The electrochemical window for each configuration demonstrated in this manuscript is as follows: LFP vs Li/Li$^+$, 2.5–4.0 V.

Material Characterization: Scanning electron microscopy (SEM) images were taken using a Thermo Fisher Quanta 650 environmental scanning electron microscope with an applied accelerating voltage of 30 kV. Small-angle X-ray scattering (SAXS) was performed on samples under vacuum using a XENOCS Ganesha SAXS-WAXS system with monochromatic Cu Kα X-rays (λ = 1.54 Å). Scattered X-rays were captured for XYZ min with a 487 × 619 pixels Pilatus3 R 300k (pixel size of 172 × 172 µm^2) detector. XPS spectra were recorded using a monochromated 120 W Al-Kα1 X-ray source (*hv* = 1486.5 eV). XPS fitting was conducted using CasaXPS software and employing a Shirley background fit. Each component was fitted using a rigid set of constraints on the peak position and full-width half-max, thereby eliminating peak fitting discrepancies between samples. The full details of peak fitting parameters can be found in the supporting information. ToF-SIMS was conducted with an ION-ToF GmbH, 2010. The lithium samples were extracted from cells after 10 complete cycles of stripping and plating at 1.0 mA cm^{-2}, 1.0 mAh cm^{-2}. Afterward, samples were rinsed with THF. To minimize damage to the SEI, samples were placed on an oversized washer and held at an approximate 45° angle. The solvent was then allowed to flow over the sample indirectly by squirting the liquid onto the metal spacer, thereby minimizing mechanical disturbance and agitation of the SEI. After washing, the sample was placed under vacuum to dry before analysis. Samples were kept under inert conditions throughout this process and were transported from the glovebox to the analysis chamber through a pressure-to-vacuum transfer vessel. For ToF-SIMS depth profiling, a Cs$^+$ ion beam (≈40 nA, 500eV) was used to sputter 300 × 300 µm areas; Cs was chosen to decrease the work function of the surface (≈2 eV) to increase the ionization probability of negatively charged secondary ions, while a Bi$^+$ analysis beam (0.4 pA, 30 keV) was raster scanned over a 100 × 100 µm areas, centered within the Cs$^+$-sputtered area, segmented into 256 × 256 pixels in high current mode. All depth profiling used a non-interlaced analysis (sequential sputtering and surface analysis). In this study, the criteria for a "peak" were classified as having an intensity >100 counts per scan and a signal: noise >1.0. Only peaks with an *m/z* range of 1.0–200.0 were analyzed to aid in effectively identifying species. Additional criteria for this analysis: peaks cannot overlap with one another, the baseline for the peak must be normal, and the depth profile of the spectra must have notable features (eliminating saturated ions, background species, etc.). The ToF-SIMS data clustering analysis was conducted using the Morpheus software from the Broad Institute (https://software.broadinstitute.org/morpheus/). Hierarchical clustering was performed using a one minus Pearson correlation metric and an average lineage method. The resulting dendrograms and degree of clustering for each spectrum are displayed in Figures S25–S32 in the Supporting Information. Similarity matrices were also created using a Pearson correlation. Integrated yield analysis was employed to obtain a quantitative comparison between the concentrations of various SEI components. By conducting ToF-SIMS depth profiles in triplicate using different locations around the postmortem sample, statistics of the composition can be made and then used to quantify the degree of spatial heterogeneity. Standard deviations for the average integrated yield of each analyzed species were created and combined to obtain an average

relative standard deviation for the entire sample. The metric acts as a method of determining chemical spatial heterogeneity within the SEI of the sample. Additional experimental details on the depth profile clustering analysis and the integrated yield analysis can be found in the Supporting Information.

Molecular Dynamic Simulations: The DFT-based AIMD (ab initio molecular dynamics) simulation employed CP2K code with the Quickstep module, using a mixed Gaussian and plane wave basis set and its augmented all-electron extension.[69] Matching the Li-salt concentration of 1.15 M and the solvent composition of THF:m-THF = 1:1 v/v in each system, the molecular composition was calculated using 10 salt molecules, 62 THF, and 50 m-THF molecules. Simulations were conducted using a box size of 27.0, 28.1, 27.3, and 26.9 Å^3 for the LiPF$_6$, LiTFSI, LiFSI, and LiDFOB, respectively. Periodic boundary conditions were applied. Each mixture was simulated under an NVT ensemble at 300 K for a simulation time of 20 ps, with a time step of 1fs, using a Langevin thermostat. To study the neighboring environment of Li$^+$, representative structures from an AIMD run were collected for the radial distribution function (RDF, $g(r)$) analysis centered on the Li atom. The coordination number for relevant atoms/molecules around Li$^+$ was calculated from the RDF via an integral transformation to $g(r)$. Structure models were visualized with VESTA.

Supporting Information

Supporting Information is available from the Wiley Online Library or from the author.

Conflict of Interest

The authors declare no conflict of interest.

Author Contributions

The manuscript was written through equal contributions of all authors. All authors have approved the final version of the manuscript.

Data Availability Statement

The data that support the findings of this study are available in the supplementary material of this article.

[1] M. V. Reddy, A. Mauger, C. M. Julien, A. Paolella, K. Zaghib, *Materials* **2020**, *13*, 1884.

[2] Z. Hu, J. Li, X. Zhang, Y. Zhu, *Front. Chem.* **2020**, *8*, 409.

[3] X. Gao, Y.-N. Zhou, D. Han, J. Zhou, D. Zhou, W. Tang, J. B. Goodenough, *Joule* **2020**, *4*, 1864.

[4] J.-G. Zhang, W. Xu, J. Xiao, X. Cao, J. Liu, *Chem. Rev.* **2020**, *120*, 13312.

[5] H. Liu, X.-B. Cheng, Z. Jin, R. Zhang, G. Wang, L.-Q. Chen, Q.-B. Liu, J.-Q. Huang, Q. Zhang, *EnergyChem* **2019**, *1*, 100003.

[6] P. Bai, J. Li, F. R. Brushett, M. Z. Bazant, *Energy Environ. Sci.* **2016**, *9*, 3221.

[7] A. Jana, S. Inn Woo, K. S. N. Vikrant, R. Edwin García, *Energy Environ. Sci.* **2019**, *12*, 3595.

[8] H. Liu, X.-B. Cheng, R. Xu, X.-Q. Zhang, C. Yan, J.-Q. Huang, Q. Zhang, *Adv. Energy Mater.* **2019**, *9*, 1902254.

[9] Z. Hong, V. Viswanathan, *ACS Energy Lett.* **2018**, *3*, 1737.

[10] L. Chen, H. W. Zhang, L. Y. Liang, Z. Liu, Y. Qi, P. Lu, J. Chen, L.-Q. Chen, *J. Power Sources* **2015**, *300*, 376.

[11] A. Mistry, C. Fear, R. Carter, C. T. Love, P. P. Mukherjee, *ACS Energy Lett.* **2018**, *4*, 156.

[12] A. Wang, S. Kadam, H. Li, S. Shi, Y. Qi, *NPJ Comput. Mater.* **2018**, *4*, 15.

[13] E. Peled, D. Golodnitsky, G. Ardel, *J. Electrochem. Soc.* **1997**, *144*, L208.

[14] R. Deshpande, M. Verbrugge, Y.-T. Cheng, J. Wang, P. Liu, *J. Electrochem. Soc.* **2012**, *159*, A1730.

[15] H.-L. Zhang, F. Li, C. Liu, J. Tan, H.-M. Cheng, *J. Phys. Chem. B* **2005**, *109*, 22205.

[16] J. D. McBrayer, C. A. Apblett, K. L. Harrison, K. R. Fenton, S. D. Minteer, *Nanotechnology* **2021**, *32*, 502005.

[17] W.-W. Wang, Y. Gu, H. Yan, S. Li, J.-W. He, H.-Y. Xu, Q.-H. Wu, J.-W. Yan, B.-W. Mao, *Chem* **2020**, *6*, 2728.

[18] H.-H. Sun, A. Dolocan, J. A. Weeks, R. Rodriguez, A. Heller, C. B. I.n Mullins, *J. Mater. Chem. A* **2019**, *7*, 17782.

[19] E. Cha, J. H. Yun, R. Ponraj, D. K. Kim, *Mater. Chem. Front.* **2021**, *5*, 6294.

[20] Y. Li, Y. Li, L. Zhang, H. Tao, Q. Li, J. Zhang, X. Yang, *J. Energy Chem.* **2023**, *77*, 123.

[21] X. Shen, H. Ji, J. Liu, J. Zhou, C. Yan, T. Qian, *Energy Storage Mater.* **2020**, *24*, 426.

[22] A. G. Scheuermann, D. Q. Lu, T. Ito, C. E. D. Chidsey, P. C. McIntyre, *ECS Trans.* **2014**, *64*, 265.

[23] S. Mehla, *J. Electron. Commun. Eng.* **2016**, *01*, 125.

[24] M. Wang, L. Huai, G. Hu, S. Yang, F. Ren, S. Wang, Z. Zhang, Z. Chen, Z. Peng, C. Shen, D. Wang, *J. Phys. Chem. C* **2018**, *122*, 9825.

[25] G. Wan, F. Guo, X. Ai, J. Qian, Y. Li, H. Yang, *ACS Appl. Mater. Interfaces* **2018**, *10*, 593.

[26] S. Liu, X. Ji, N. Piao, J. Chen, N. Eidson, J. Xu, P. Wang, L. Chen, J. Zhang, T. Deng, S. Hou, T. Jin, H. Wan, J. Li, J. Tu, C. Wang, *Angew. Chem., Int. Ed.* **2021**, *60*, 3661.

[27] G. Bieker, M. Winter, P. Bieker, *Phys. Chem. Chem. Phys.* **2015**, *17*, 8670.

[28] E. W. C. Spotte-Smith, R. L. Kam, D. Barter, X. Xie, T. Hou, S. Dwaraknath, S. M. Blau, K. A. Persson, *ACS Energy Lett.* **2022**, *7*, 1446.

[29] E. W. C. Spotte-Smith, T. B. Petrocelli, H. D. Patel, S. M. Blau, K. A. Persson, *ACS Energy Lett.* **2022**, *8*, 347.

[30] J. Chen, X. Fan, Q. Li, H. Yang, M. R. Khoshi, Y. Xu, S. Hwang, L. Chen, X. Ji, C. Yang, H. He, C. Wang, E. Garfunkel, D. Su, O. Borodin, C. Wang, *Nat. Energy* **2020**, *5*, 386.

[31] A. G. Paul-Orecchio, J. A. Weeks, A. Dolocan, C. B. Mullins, *ACS Appl. Energy Mater.* **2022**, *5*, 9437.

[32] J. Chen, Q. Li, T. P. Pollard, X. Fan, O. Borodin, C. Wang, *Mater. Today* **2020**, *39*, 118.

[33] T. D. Pham, A. Bin Faheem, K.-K. Lee, *Small* **2021**, *17*, 2103375.

[34] M. Li, C. Wang, Z. Chen, K. Xu, J. Lu, *Chem. Rev.* **2020**, *120*, 6783.

[35] L. Su, E. Jo, A. Manthiram, *ACS Energy Lett.* **2022**, *7*, 2165.

[36] Y. Zheng, F. A. Soto, V. Ponce, J. M. Seminario, X. Cao, J.-G. Zhang, P. B. Balbuena, *J. Mater. Chem. A* **2019**, *7*, 25047.

[37] L. Su, H. Charalambous, Z. Cui, A. H.-E. Manthiram, *Energy Environ. Sci.* **2022**, *15*, 843.

[38] X. Cao, H. Jia, W. Xu, J.-G. Zhang, *J. Electrochem. Soc.* **2021**, *168*, 010522.

[39] S. Angarita-Gomez, P. B. Balbuena, *Mater. Adv.* **2022**, *3*, 6352.

[40] S. Tobishima, T. Okada, *Electrochim. Acta* **1985**, *30*, 1715.

[41] E. R. Logan, E. M. Tonita, K. L. Gering, J. Li, X. Ma, L. Y. Beaulieu, J. R. Dahn, *J. Electrochem. Soc.* **2018**, *165*, A21.

[42] A. J. Ringsby, K. D. Fong, J. Self, H. K. Bergstrom, B. D. McCloskey, K. A. Persson, *J. Electrochem. Soc.* **2021**, *168*, 080501.

[43] K. Qian, R. E. Winans, T. Li, *Adv. Energy Mater.* **2021**, *11*, 2002821.

[44] K. Qian, S. Seifert, R. E. Winans, T. Li, *Energy Fuels* **2021**, *35*, 19849.

[45] J. Huang, M. Papac, R. O'Hayre, *Electrochim. Acta* **2021**, *367*, 137493.

[46] Y. Zhao, V. Kumtepeli, S. Ludwig, A. Jossen, *J. Power Sources* **2022**, *530*, 231250.

[47] J. Becherer, D. Kramer, R. Mönig, *J. Mater. Chem. A* **2022**, *10*, 5530.

[48] S. Nanda, A. Gupta, A. Manthiram, *Adv. Energy Mater.* **2021**, *11*, 2000804.

[49] Y. Xiao, R. Xu, L. Xu, Y.-X. Zhan, J.-F. Ding, S. Zhang, Z.-H. Li, C. Yan, J.-Q. Huang, *Adv. Energy Mater.* **2023**, *13*, 2300959.

[50] H. Xu, Z. Li, T. Liu, C. Han, C. Guo, H. Zhao, Q. Li, J. Lu, K. Amine, X. Qiu, *Angew. Chem., Int. Ed.* **2022**, *61*, 202202894.

[51] M. Mao, X. Ji, Q. Wang, Z. Lin, M. Li, T. Liu, C. Wang, Y.-S. Hu, H. Li, X. Huang, L. Chen, L. Suo, *Nat. Commun.* **2023**, *14*, 1082.

[52] H. Shin, J. Park, S. Han, A. M. Sastry, W. Lu, *J. Power Sources* **2015**, *277*, 169.

[53] V. V. Brazhkin, E. L. Gromnitskaya, I. V. Danilov, Y. Katayama, A. G. Lyapin, S. V. Popova, *Mater. Res. Express* **2015**, *2*, 025201.

[54] T. J. Young, M. A. Monclus, T. L. Burnett, W. R. Broughton, S. L. Ogin, P. A. Smith, *Meas. Sci. Technol.* **2011**, *22*, 125703.

[55] S. Hull, T. W. D. Farley, W. Hayes, M. T. Hutchings, *J. Nucl. Mater.* **1988**, *160*, 125.

[56] J. H. Strange, S. M. Rageb, A. V. Chadwick, K. W. Flack, J. H. Harding, *J. Chem. Soc., Faraday Trans.* **1990**, *86*, 1239.

[57] S. Lorger, R. Usiskin, J. Maier, *J. Electrochem. Soc.* **2019**, *166*, A2215.

[58] Z. Wu, C. Wang, Z. Hui, H. Liu, S. Wang, S. Yu, X. Xing, J. Holoubek, Q. Miao, H. L. Xin, P. Liu, *Nat. Energy* **2023**, *8*, 340.

[59] M. de Jong, W. Chen, T. Angsten, A. Jain, R. Notestine, A. Gamst, M. Sluiter, C. Krishna Ande, S. van der Zwaag, J. J. Plata, C. Toher, S. Curtarolo, G. Ceder, K. A. Persson, M. Asta, *Sci. Data* **2015**, *2*, 150009.

[60] M. J. Zachman, Z. Tu, S. Choudhury, L. A. Archer, L. F. Kourkoutis, *Nature* **2018**, *560*, 345.

[61] R. A. Vilá, D. T. Boyle, A. Dai, W. Zhang, P. Sayavong, Y. Ye, Y. Yang, J. A. Dionne, Y. Cui, *Sci. Adv.* **2023**, *9*, eadf3609.

[62] M. M. Islam, T. Bredow, P. Heitjans, *J. Phys.: Condens. Matter* **2012**, *24*, 203201.

[63] M. M. Islam, T. Bredow, P. Heitjans, *J. Phys. Chem. C* **2011**, *115*, 12343.

[64] I. Petousis, D. Mrdjenovich, E. Ballouz, M. Liu, D. Winston, W. Chen, T. Graf, T. D. Schladt, K. A. Persson, F. B. Prinz, *Sci. Data* **2017**, *4*, 160134.

[65] H. S. Jadhav, M.-S. Cho, R. S. Kalubarme, J.-S. Lee, K.-N. Jung, K.-H. Shin, C.-J. Park, *J. Power Sources* **2013**, *241*, 502.

[66] B. S. Parimalam, B. L. Lucht, *J. Electrochem. Soc.* **2018**, *165*, A251.

[67] H. Wu, B. Tang, X. Du, J. Zhang, X. Yu, Y. Wang, J. Ma, Q. Zhou, J. Zhao, S. Dong, G. Xu, J. Zhang, H. Xu, G. Cui, L. Chen, *Adv. Sci.* **2020**, *7*, 2003370.

[68] C. Fu, V. Venturi, J. Kim, Z. Ahmad, A. W. Ells, V. Viswanathan, B. A. Helms, *Nat. Mater.* **2020**, *19*, 758.

[69] T. D. Kühne, M. Iannuzzi, M. Del Ben, V. V. Rybkin, P. Seewald, F. Stein, T. Laino, R. Z. Khaliullin, O. Schütt, F. Schiffmann, D. Golze, J. Wilhelm, S. Chulkov, M. H. Bani-Hashemian, V. Weber, U. Borštnik, M. Taillefumier, A. S. Jakobovits, A. Lazzaro, H. Pabst, T. Müller, R. Schade, M. Guidon, S. Andermatt, N. Holmberg, G. K. Schenter, A. Hehn, A. Bussy, F. Belleflamme, G. Tabacchi, et al., *J. Chem. Phys.* **2020**, *152*, 194103.